Cancer Cell

Article

Activated T cell extracellular vesicle DNA transfer enhances antigen presentation and anti-tumor immunity

Graphical abstract

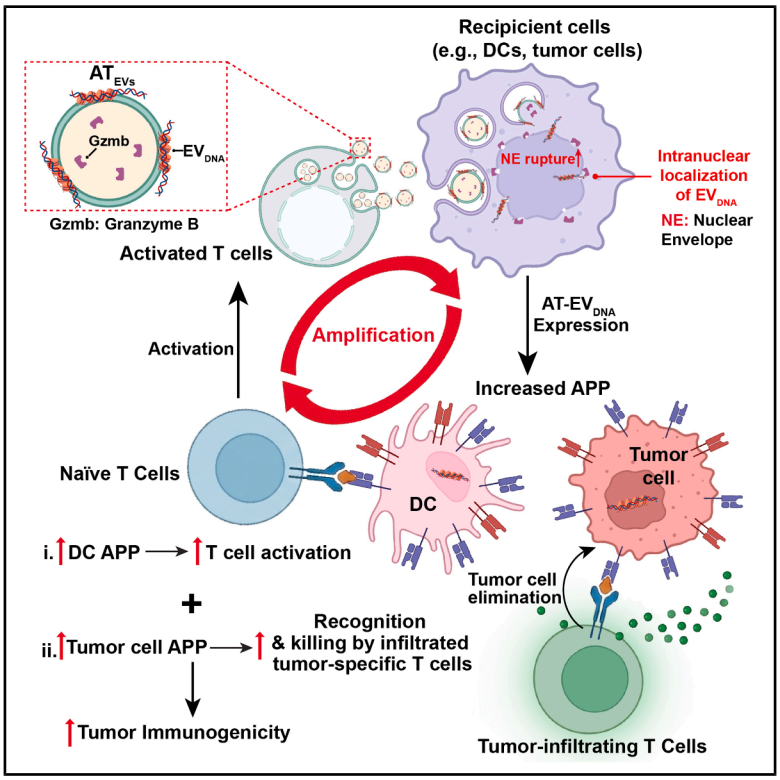

Highlights

- Activated T cells secrete abundant extracellular vesicular DNA (AT-EV_{DNA})
- AT-EV_{DNA} is mainly from newly made genomic DNA rich in immune-related gene content
- AT_{EVs} boost antigen presentation via EV_{DNA} intranuclear transfer aided by granzyme B
- AT_{EVs} act as acellular immunotherapy to overcome tumor immune evasion

Authors

Mengying Hu, Di-Ao Liu, Inbal Wortzel, ..., Haiying Zhang, Irina R. Matei, David Lyden

Correspondence

haz2005@med.cornell.edu (H.Z.), irm2224@med.cornell.edu (I.R.M.), dcl2001@med.cornell.edu (D.L.)

In brief

Hu et al. identify an intercellular communication mechanism by which activated T cell-derived EVs (AT_{EVs}) enhance or restore antigen processing and presentation (APP) in dendritic and tumor cells. This immunogenicity is driven by granzyme B-facilitated nuclear transfer of EV-DNA enriched in APP genes, positioning AT_{EVs} as a promising acellular immunotherapy to overcome immune evasion and boost checkpoint blockade.

Hu et al., 2026, Cancer Cell *44*, 965–982
May 11, 2026
https://doi.org/10.1016/j.ccell.2026.03.023

CellPress

Cancer Cell

CellPress
OPEN ACCESS

Article

Activated T cell extracellular vesicle DNA transfer enhances antigen presentation and anti-tumor immunity

Mengying Hu,[1,2,22] Di-Ao Liu,[1,22] Inbal Wortzel,[1] Paul Collier,[3] Theodore M. Nelson,[3] Jonathan Foox,[3] Guojie Zhong,[4] Gabriel Tobias,[1] Tetsuhiko Asao,[1,5,6] Linda Bojmar,[1,7] Candia M. Kenific,[1] Gang Wang,[1] Simone Caielli,[8] Zurong Wan,[8] Sarah Qureshy,[1] Max Reed,[1] Richard Piszczatowski,[1] Purnima Ravisankar,[8] Julia A. Brown,[8] Sihan Xiong,[1] Huajuan Wang,[1] Pernille Lauritzen,[1] Yael Aylon,[9] Henrik Molina,[10] William R. Jarnagin,[11] Moshe Oren,[9] Ben Z. Stanger,[12] Jack Bui,[13] Gabriele Bergers,[14] Agnès Noël,[15] Paul M. Grandgenett,[16] Michael A. Hollingsworth,[16] David Tuveson,[17] Nancy Boudreau,[1] Jacqueline Bromberg,[18] David Kelsen,[19] David R. Jones,[5] Laura Santambrogio,[20] Melody Y. Zeng,[8] Virginia Pascual,[8] Han Sang Kim,[1,21] Christopher E. Mason,[3] Haiying Zhang,[1,*] Irina R. Matei,[1,*] and David Lyden[1,23,*]

[1]Children's Cancer and Blood Foundation Laboratories, Departments of Pediatrics, and Cell and Developmental Biology, Drukier Institute for Children's Health, Meyer Cancer Center, Weill Cornell Medicine, New York, NY, USA
[2]Division of Pharmaceutics and Pharmacology, College of Pharmacy, The Ohio State University, Columbus, OH, USA
[3]Department of Physiology, Biophysics, and Systems Biology, Weill Cornell Medicine, New York, NY, USA
[4]Department of Systems Biology, Columbia University, New York, NY, USA
[5]Thoracic Surgery Service, Department of Surgery, Memorial Sloan Kettering Cancer Center, New York, NY, USA
[6]Department of Respiratory Medicine, Juntendo University, Tokyo, Japan
[7]Department of Biomedical and Clinical Sciences, Linköping University, Linköping, Sweden
[8]Drukier Institute for Children's Health and Department of Pediatrics, Weill Cornell Medicine, New York, NY, USA
[9]Department of Molecular Cell Biology, The Weizmann Institute of Science, Rehovot, Israel
[10]Proteomics Resource Center, The Rockefeller University, New York, NY 10065, USA
[11]Hepatopancreatobiliary Service, Department of Surgery, Memorial Sloan Kettering Cancer Center, New York, NY, USA
[12]Department of Medicine, Perelman School of Medicine, University of Pennsylvania, Philadelphia, PA, USA
[13]Department of Pathology, University of California, San Diego, La Jolla, CA, USA
[14]Laboratory of Tumor Microenvironment and Therapeutic Resistance, KU Leuven, Leuven, Belgium
[15]Laboratory of Biology of Tumor and Development, Université de Liège, Liège, Belgium
[16]Eppley Institute for Research in Cancer and Allied Diseases, Fred & Pamela Buffett Cancer Center, University of Nebraska Medical Center, Omaha, NE, USA
[17]Cancer Center, Cold Spring Harbor Laboratory, Cold Spring Harbor, New York, NY 11724, USA
[18]Department of Medicine, Memorial Sloan Kettering Cancer Center, New York, NY, USA
[19]Gastrointestinal Oncology Service, Memorial Sloan Kettering Cancer Center, New York, NY, USA
[20]Department of Radiation Oncology, Weill Cornell School of Medicine, New York, NY, USA
[21]Yonsei Cancer Center, Division of Medical Oncology, Department of Internal Medicine, Yonsei University College of Medicine, Seoul, South Korea
[22]These authors contributed equally
[23]Lead contact
*Correspondence: haz2005@med.cornell.edu (H.Z.), irm2224@med.cornell.edu (I.R.M.), dcl2001@med.cornell.edu (D.L.)
https://doi.org/10.1016/j.ccell.2026.03.023

SUMMARY

Antigen processing and presentation (APP) is essential for adaptive immunosurveillance. We uncover a mechanism whereby activated T cell-derived extracellular vesicles (AT_{EVs}) drive a positive feedback loop that enhances antigen presentation and immune responses in normal physiology and cancer. AT_{EV}-induced immunogenicity relies on extracellular vesicular double-stranded DNA (EV_{DNA}), which is notably abundant and primarily composed of genomic DNA enriched in immune-related genes, including those encoding APP machinery. Mechanistically, granzyme B (Gzmb) packaged by AT_{EVs} disrupts the nuclear envelope of recipient cells, facilitating intranuclear transfer and subsequent transient expression of EV_{DNA} encoding APP genes. DNase treatment removes most AT-EV_{DNA}, abrogating APP upregulation and thus T cell activation and recruitment to tumors. Notably, AT_{EVs} hold promise as an acellular immunotherapy, restoring APP and synergizing with checkpoint blockade in immunotherapy-refractory tumors. Collectively, our findings uncover a mechanism of transient, non-viral gene delivery by AT_{EVs} that boosts APP and anti-tumor immunity while limiting autoimmunity.

INTRODUCTION

Over the past decade, immunotherapies have revolutionized cancer treatment, significantly improving patient survival.[1] Effective anti-tumor immunity relies on major histocompatibility complex (MHC)-dependent tumor antigen recognition by cytotoxic $CD8^+$ T cells and activation of their cell-killing functions. Successful antigen presentation first involves tumor antigen uptake by antigen-presenting cells (APCs), such as dendritic cells (DCs), followed by $CD8^+$ T cell priming and recognition of MHC class I (MHC-I)-bound antigen.[2] Tumors often evade immune surveillance by disrupting antigen processing and presentation (APP) and expressing inhibitory signals, such as PD-L1, that suppress tumor-specific T cells. While immune checkpoint inhibitors (ICIs) can restore T cell activity,[3,4] tumors often downregulate or lose MHC expression,[5–7] disrupt key genes involved in antigen proteolysis, delivery, and loading onto MHC molecules,[8–10] and secrete immunosuppressive factors that impair DC cross-presentation.[11–14] Thus, the disruption of the APP machinery is a key driver of poor immunogenicity and low response rates to immunotherapy in most cancer types.[15,16] To date, interferon (IFN), particularly IFN-γ signaling is the sole known mechanism upregulating APP pathways in immune cells,[17] yet its complex and opposing roles in the tumor microenvironment have limited its efficacy in cancer treatment.[18–20] Therefore, identifying alternative mechanisms to enhance tumor antigen presentation could lead to more effective anti-tumor immune responses.

Extracellular vesicles (EVs) are nanoparticles naturally released by all living cells, containing proteins, lipids, and genetic material, that facilitate intercellular communication.[21] EVs carry both genomic DNA (gDNA)[22] and mitochondrial DNA (mtDNA)[23] located both inside and on the surface of EVs, but the function of extracellular vesicular DNA (EV_{DNA}) remains underexplored. Our recent work highlighted the pivotal role of immune developmental pathways and genes in regulating EV_{DNA} packaging in various tumor cell types, and demonstrated how tumor-derived EV_{DNA} primes Kupffer cell-mediated antitumor immunity to prevent metastatic progression.[24] This raised the possibility that EV_{DNA} from immune cells, such as T cells, may also have immune-related functions.

T cell receptor interaction with cognate MHC loaded with antigenic peptides leads to T cell activation and differentiation.[25] However, the role of activated T cell EVs in interactions with APCs or tumor cells has yet to be elucidated. Here, by characterizing the molecular cargo of activated T cell EVs and the functional impact of AT-EV_{DNA}, we uncover a mechanism of augmenting APP in both physiological and pathological contexts. These findings reveal the translational potential of activated T cell-derived extracellular vesicles (AT_{EVs}) by exploiting a naturally occurring immune-boosting process to overcome immune evasion, particularly in immunologically silent cancers.

RESULTS

Activated T cell-derived EVs enhance DC antigen presentation under homeostatic conditions

Adaptive-innate crosstalk is classically mediated by juxtacrine signaling[26,27] or soluble cytokines and chemokines.[28,29] EVs have recently emerged as an additional contact-independent communication mechanism[30] via the transfer of proteins, lipids, and nucleic acids.[31,32] Thus, we tested whether T cell-derived EVs participate in crosstalk with APCs and orchestrate systemic immunity under physiological conditions.

$CD45^+CD3^+$ T cells from mouse spleens and lymph nodes (LNs) were cultured *ex vivo* with or without IL-2 and anti-CD3/CD28 stimulation for EV collection.[32–34] To minimize contamination from apoptotic cells, non-activated T cell-derived EVs (NT_{EVs}) were isolated from Day 3 supernatants, when >90% of cells were viable (Figure S1A). T cell activation occurred within 3 days, as indicated by increased CD5 and CD25 expression (Figure S1A), and retained viability through Day 9. Supernatants from Days 6 and 9 at peak expansion were pooled for AT_{EV} isolation.

Electron microscopy (EM), nanoparticle tracking analyses, and Zetasizer characterization identified heterogeneous vesicles with a mode size of ∼150 nm and a slightly negative surface charge (Figure S1B). In healthy mice, near-infrared dye-labeled EVs, irrespective of source, predominantly accumulated in the liver and spleen (Figures S1C and S1D). Relative to EVs derived from non-immune cells, such as fibroblasts, NT_{EVs} and AT_{EVs} exhibited enhanced biodistribution to immune organs, including the thymus, spleen, bone, and most prominently the LNs (Figure 1A). Flow cytometry further revealed preferential uptake of AT_{EVs} and NT_{EVs} by $CD11c^+$ DCs in LNs (Figures 1B and S1E). Immunofluorescence microscopy confirmed co-localization of labeled AT_{EVs} with DCs in the LNs and spleen (Figure 1C and S1F–S1H).

To study the functional effects of T cell-derived EVs on lymph node DCs (LN-DCs), we performed RNA sequencing (RNA-seq) on DCs from cervical LNs after three intravenous (i.v.) injections of NT_{EVs} or AT_{EVs} administered every other day (Figures S2A and S2B). Gene set enrichment analysis (GSEA) of differentially expressed genes (DEGs) in AT_{EV}^- and NT_{EV}^-treated DCs relative to PBS controls revealed broad enrichment of immune-related signatures, including Fc receptor signaling, complement cascade, scavenger receptor engagement, infection, innate and adaptive immune, and immunoregulatory pathways, as well as trafficking-related pathways, such as extracellular matrix remodeling, hemostasis, vesicle-mediated transport, and cellular adhesion and migration. Notably, AT_{EVs} uniquely upregulated APP pathways (Figures S2C and S2D). Compared with NT_{EV} treatment, APP was the top-enriched pathway in AT_{EV}-treated LN-DCs, whereas glycosylation, keratinization, and phospholipid metabolism pathways were enriched in NT_{EV}-treated cells (Figure S2E). The volcano plot of DEGs in AT_{EV}- versus NT_{EV}-treated DCs showed that MHC molecules and genes encoding APP machinery were highly represented among the top 20 significantly upregulated genes (Figure 1D). Consistently, the expression of most MHC molecules, MHC-I and MHC-II transactivators (*Nlrc5* and *Ciita*), immunoproteasome components (*Psmb8* and *Psmb9*), and peptide-loading complex components (*Tap1*, *Tap2*, *Tapbp*, *Tapbpl*, *Cd74*) was significantly upregulated in AT_{EV}-treated LN-DCs compared with either PBS- or NT_{EV}-treated cells (Figure S2F). Similar results were observed following *in vitro* treatment of DC2.4 cells (immortalized murine DCs) (Figures S2G–S2K). To verify our findings in an antigen-specific context, OT-II T cells were co-cultured with irradiated bone marrow-derived DCs (BMDCs) pre-loaded with

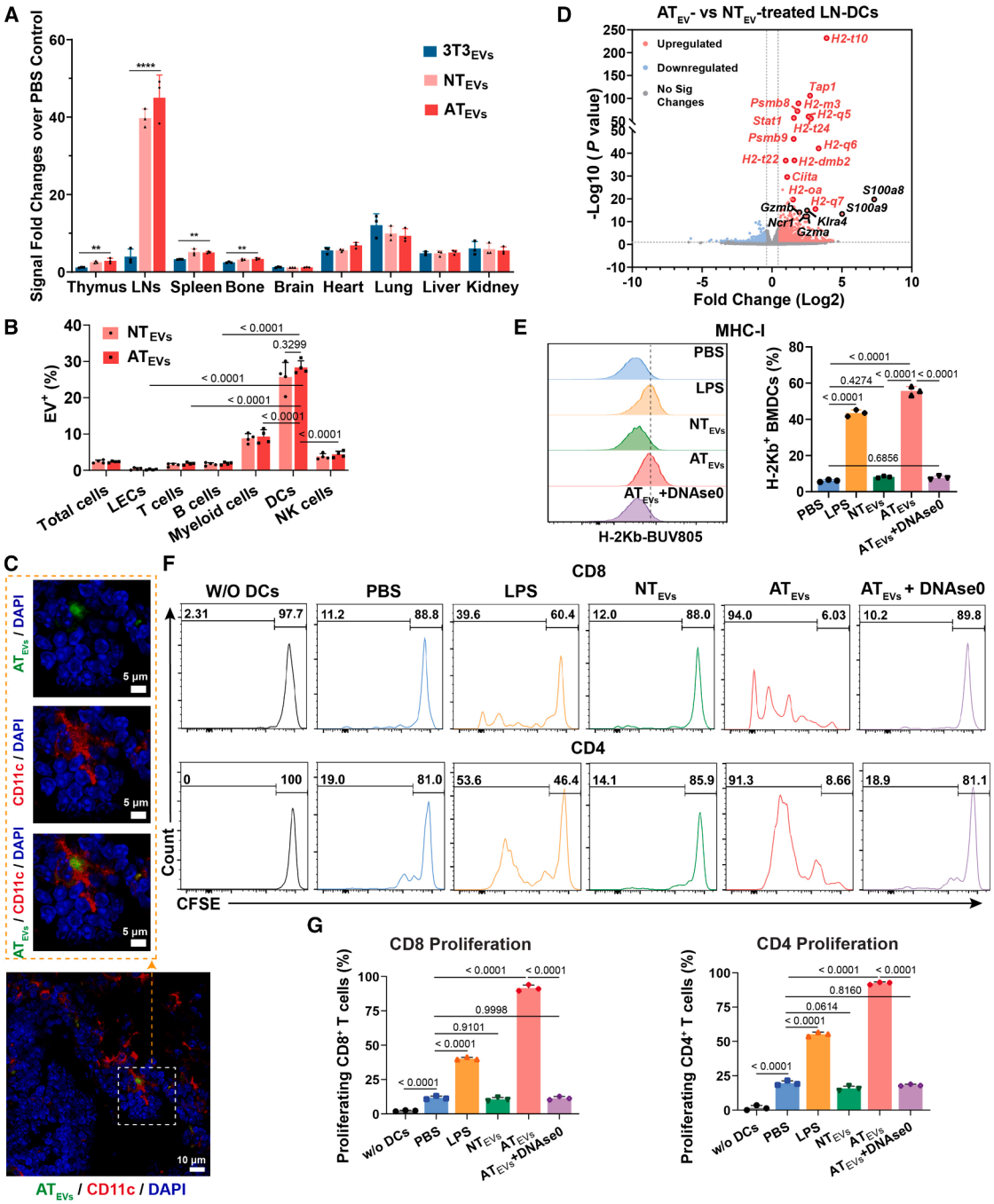

Figure 1. T cell-derived EVs biodistribution and function under physiological conditions

(A) Fold-change analysis of NIR815-labeled EV biodistribution across organs 24h after retro-orbital i.v. injection in naive mice, quantified based on whole-organ Odyssey images (Image Studio) and normalized to organ size. Fold changes were calculated by comparing experimental groups with PBS controls (n = 3 per group).

(B) Flow cytometric analysis of the frequencies of indicated cell subpopulations that uptake NT_{EVs} or AT_{EVs} in cervical LNs 24h after the retro-orbital i.v. injection of CellVue Burgundy-labeled NT_{EVs} or AT_{EVs} into naive mice. LECs, lymphatic endothelial cells ($CD45^-CD31^+$); T cells ($CD45^+CD3^+B220^-$); B cells ($CD45^+B220^+CD3^-$); Myeloid cells ($CD45^+CD3^-B220^-CD11c^-CD11b^+$); DCs ($CD45^+CD3^-B220^-CD11c^+$); NK cells ($CD45^+CD3^-B220^-CD11c^-CD11b^-NK1.1^+$) ($n$ = 4 per group).

(C) Representative immunofluorescence images of $CD11c^+$ cells and CellVue Jade-labeled AT_{EV} co-localization in cervical LNs. Scale bars, 10 μm and 5μm for magnified images.

(D) Volcano plot of DEGs between AT_{EV}^- and NT_{EV}^-treated LN-DCs. Dashed lines indicate the threshold of significant differential gene expression, defined as $\log_2$ fold change < −0.5 and >0.5 with −log10(P) > 1.301. Top 20 significantly upregulated genes are depicted; APP-associated genes are highlighted in red.

(E) Flow cytometric detection of H-$2K^b$ on C57BL/6 BMDCs treated with PBS, NT_{EVs}, AT_{EVs}, and DNAse0-pretreated AT_{EVs} (n = 3 mice).

(legend continued on next page)

OVA peptide (BMDC-OVA$^+$) or left unloaded (BMDC-OVA$^-$). EVs from BMDC-OVA$^+$-activated T cells significantly upregulated MHC expression in recipient DC2.4 cells compared to EVs from T cell-BMDC-OVA$^-$ co-cultures (non-activated control), reaching levels comparable to those induced by AT_{EVs} from bead-activated T cells (Figure S2L).

Functionally, AT_{EVs} induced more potent activation of BMDCs than lipopolysaccharide (LPS), evidenced by > 10-fold higher expression of CD86, whereas NT_{EVs} had minimal effect (Figure S3A). While AT_{EVs} alone did not directly activate allogenic T cells (Figure S3B), BMDCs primed with AT_{EVs} significantly increased MHC-I/II expression (Figures 1E and S3C) and drove robust allogeneic CD4$^+$ and CD8$^+$ T cell proliferation and activation, as indicated by CFSE dilution and CD69 upregulation, respectively (Figures 1F, 1G, and S3D). Similar trends were observed in BlaER1 monocytes treated with human T cell EVs (Figure S3E).[35] Together, AT_{EVs}, but not NT_{EVs}, enhance DC antigen presentation via contact-independent mechanisms.

EV_{DNA} mediates the immune-boosting effects of AT_{EVs}

To identify the AT_{EV} cargo driving the immune-stimulatory effect, we characterized EV proteins and nucleic acids. While EV protein (2-6 $\times 10^{-9}$ μg particle^{-1}) and RNA levels were similar across cell types (Figures S4A–S4C), EVs from neutrophils and adaptive immune cells, including primary T cells and CD40-activated B cells, contained exceptionally higher levels of DNA compared with EVs from macrophages, DCs, fibroblasts, or tumor cell lines (Figures 2A, S4D, and S4E). T cell activation, by anti-CD3/CD28 beads or antigen-pulsed BMDCs, further increased EV_{DNA} level relative to non-activated T cells (Figures S4B, S4D, and S4E), regardless of the normalization approach (protein or particle count), consistent with our previous discovery linking immune developmental genes to EV_{DNA} packaging.[24] Lymphoma (TK1) and leukemia cell lines (Jurkat and NALM-6) have EV_{DNA} levels comparable to solid tumor cell lines. Since the amount of T cell-derived EV_{RNA} was one to two orders of magnitude lower than EV_{DNA} and did not differ between NT_{EVs} and AT_{EVs} after normalization (Figures S4E and S4F), we focused on EV_{DNA} cargo in subsequent studies. Next, we quantified EV_{DNA} secretion by T cells isolated from thymus (~80% immature[36]) and peripheral lymphoid organs across T cell lineages. LN or spleen T cells secreted slightly more EV_{DNA} than thymocytes, with no differences between LN and spleen T cells, regardless of activation status, after normalization (Figure S4G). A small but significant difference in EV_{DNA} levels was observed between CD4$^+$ and CD8$^+$ T cells (Figure S4H). Therefore, pooled pan T cells from spleen and LN were used for subsequent studies.

Double-stranded DNA (dsDNA) is the predominant EV_{DNA} species.[22] Immuno-gold EM revealed dsDNA on both activated T cell-derived small EVs and non-membranous exomere particles (Figure 2B).[37] Super-resolution imaging (d-STORM) showed that ~19% and ~38% of tetraspanin$^+$ (either CD9$^+$, CD81$^+$, or CD9$^+$CD81$^+$) human NT_{EVs} and AT_{EVs}, respectively, carry dsDNA (Figure 2C). T cell-derived EV_{DNA} is fragmented, with a wide size distribution, between 150bp to 20kb, and peaks at 2kb (Figure 2D). Baseline-ZERO DNase (DNAse0), which digests both dsDNA and single-stranded DNA, did not alter AT_{EV} morphology (Figure S4I), but reduced EV_{DNA} by 70% (Figure S4J) and extensively depleted DNA species larger than 1kb (Figure 2D), indicating that T cell-derived EV_{DNA} is predominantly surface-associated and the external DNA is enriched in larger DNA fragments.

Whole genome sequencing (WGS) revealed that T cell-derived EV_{DNA} is >99.99% nuclear rather than mitochondrial (Figure S4K), with genome-wide coverage (Figure S4L). Compared to NT-EV_{DNA}, AT-EV_{DNA} exhibited increased copy number at loci corresponding to genes transcriptionally upregulated in AT_{EV}-educated relative to NT_{EV}-educated DCs across all chromosomes (Figure S4M), including many APP genes on chromosome 17. Gene ontology (GO) analysis of genes enriched in AT_{EVs} relative to NT_{EVs} (Table S1) identified APP pathways as top hits (Figure 2E). The genes driving these pathways include *H2-ob, H2-q10, Tap1, H2-ab1, H2-t5, H2-k1, Fcgr1, H2-eb1, Psmb9, Treml4, Hfe, H2-dmb2, H2-t3, H2-d1, H2-aa, H2-q2, H2-dmb1, Fcgr4, H2-eb2, Fcgr3, Flt3, H2-q1,* and *Ifng*. Importantly, the entire gene region, including the respective promoter region, was detected in AT-EV_{DNA} (Figure S5A). Quantitative PCR (qPCR) further confirmed higher relative copy numbers of MHC and other APP genes in AT-EV_{DNA} relative to NT-EV_{DNA} in both mouse and human samples (Figures 2F and S5B). This enrichment was consistent across activation methods (Figure S5C), suggesting that APP upregulation in recipient cells may be mediated by AT-EV_{DNA} delivering increased copy numbers of these genes.

AT- and NT-gDNA showed no copy number variations (Figure S6A), indicating that EV_{DNA} release does not deplete donor genomic copies. In bromodeoxyuridine (BrdU) pulse-chase experiments, BrdU remained incorporated in gDNA at 24h and 72h after withdrawal, with more than 60% of the signal persisting at 72h, confirming active cell proliferation and DNA synthesis. In contrast, the EV_{DNA} BrdU signal dropped to ~7.7% at 72h compared to 24h (Figure 2G). Non-activated T cells, which do not proliferate, did not incorporate BrdU in either their gDNA or EV_{DNA}. These findings suggest that newly synthesized DNA contributes to AT-EV_{DNA}.

Proteomic profiling of AT_{EVs} and NT_{EVs} identified histones as the most abundant proteins in both AT_{EVs} and NT_{EVs} (Figure S6B), consistent with our previous observation of chromatinized EV_{DNA}.[24] AT_{EVs} were also enriched for transcription- and translation-related proteins, presumably due to T cell activation, while only one immune-related pathway, IL-12 signaling, was enriched in NT_{EVs} (Figure S6C). Investigating the contribution of AT_{EV} proteins to APP upregulation revealed that only MHC-I molecules were present in both AT_{EVs} and NT_{EVs} and slightly elevated in AT_{EVs} (Figure S6D), but they failed to directly activate allogenic T cells (Figure S3B). MHC-II and key APP

(F, G) Alloactivation of naive BALB/c CD8$^+$ and CD4$^+$ T cells by BMDCs from (E). Proliferation was measured by CFSE dilution. F, representative histograms. G, cumulative data (n = 3 mice).

Significant differences were measured using a one-way ANOVA with the Tukey test (A, E, G) and a two-way ANOVA with the Tukey test (B). Data represent mean ± s.d. $^{**}p < 0.01$, $^{****}p < 0.0001$, or p-values are explicitly indicated.

See also Figures S1–S3.

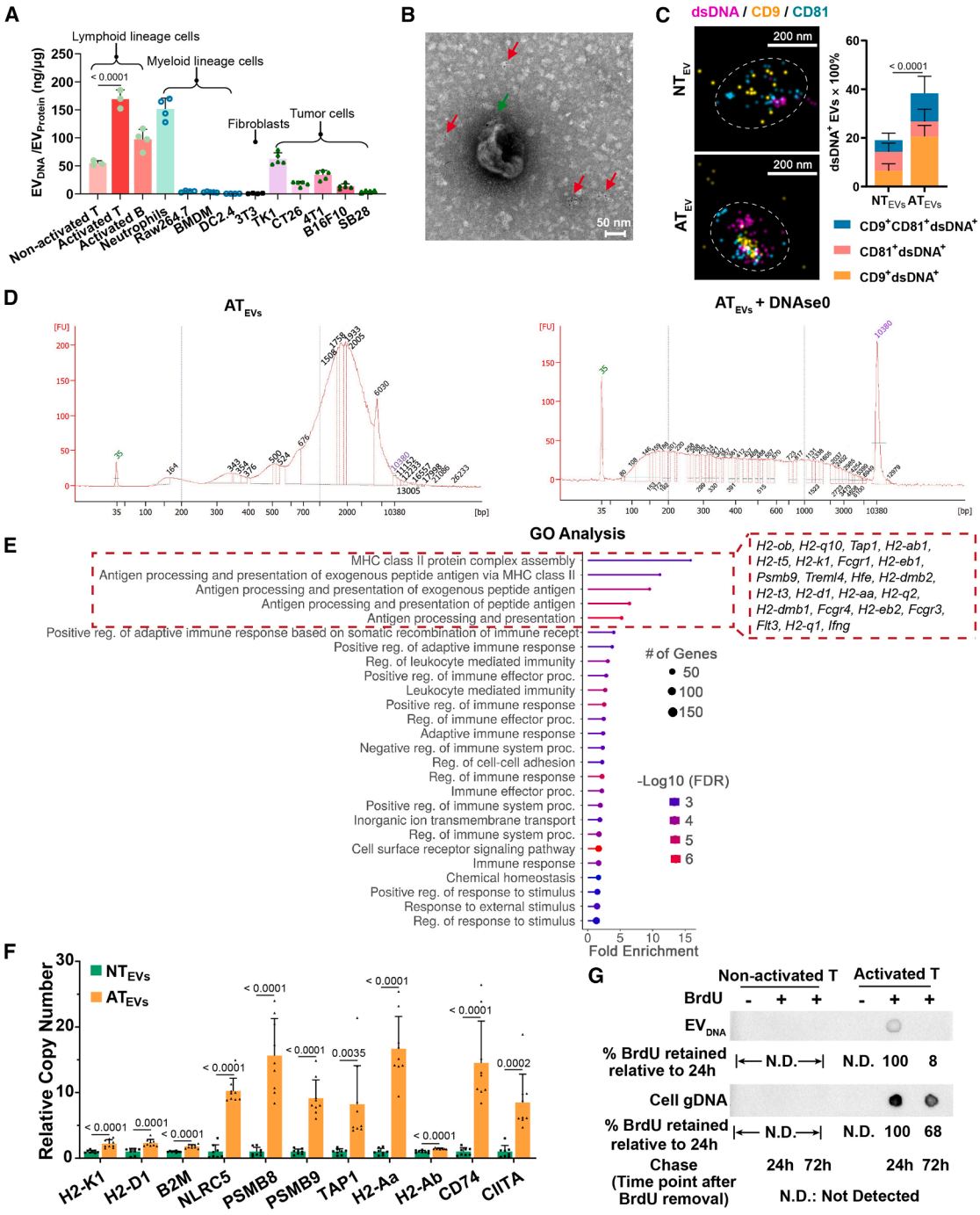

Figure 2. Characterization of T cell-derived EV_{DNA}

(A) $EV_{protein}$ normalized EV_{DNA} secreted from different murine cell types (n = 4 or 5). BMDM, bone marrow-derived macrophages.

(B) Representative TEM image of anti-dsDNA immunogold-labeled AT_{EVs}. Arrows indicate EV_{DNA} distribution across EV subpopulations (Red, exomeres; Green, exosomes). Scale bars, 50nm.

(C) Representative dSTORM image (left) of a single NT_{EV} or AT_{EV} particle (white dashed circle) stained with anti-dsDNA (Alexa Fluor 647), anti-CD9 (Alexa Fluor 488), and anti-CD81 (CF568). Scale bars, 200nm. Frequencies of $dsDNA^+CD9^+$, $dsDNA^+CD81^+$, $dsDNA^+CD9^+CD81^+$ particles relative to total tetraspanin$^+$ particles ($CD9^+$ and/or $CD81^+$) were quantified in 2–3 randomly selected fields/sample for human NT_{EVs} and AT_{EVs} (right) (n = 2).

(D) Representative electropherograms of EV_{DNA} size profiling for AT_{EVs} (left) and DNAse0-pretreated AT_{EVs} (right) by Agilent Bioanalyzer. The peaks at 35bp and 10,380 bp are internal size markers.

(E) GO analysis of genes with enriched copies in AT_{EVs} relative to NT_{EVs}. Genes driving APP-associated pathways are listed (red dashed box).

(F) Q-PCR quantification of APP-associated gene copy numbers in mouse AT-EV_{DNA} relative to NT-EV_{DNA} (n = 8).

(legend continued on next page)

proteins, such as TAPs and PSMBs, were absent in both AT_{EVs} and NT_{EVs}. Hence, AT_{EV} APP machinery proteins likely have a limited role in the effects observed in recipient DCs. Critically, DNAse0 pre-treatment abolished AT_{EV}-driven APP gene upregulation in LN-DCs and DC2.4 cells (Figures S2F and S2K), and broadly compromised enrichment of immune stimulatory pathways (Figures S6E and S6F). DNAse0 also eliminated AT_{EV}-mediated MHC upregulation in BMDCs and human BlaER1 monocytes (Figures 1E, S3C, and S3E) and impaired the subsequent allogenic $CD4^+$ and $CD8^+$ T cell proliferation (Figures 1F, 1G, and S3D). Collectively, these findings indicate that newly synthesized, APP-coding region-enriched AT-EV_{DNA} is essential for AT_{EVs}' immunostimulatory function.

AT_{EVs} directly enhance tumor cell immunogenicity by promoting MHC upregulation

Tumors reduce immunogenicity through multiple mechanisms, including transcriptional and epigenetic downregulation of APP-associated genes,[9,10] post-translational degradation of surface MHC-I,[5] and altered INF-γ signaling.[38] Given that AT_{EVs} enhance antigen presentation in DCs, we sought to test whether AT_{EVs} also promote tumor immunogenicity, particularly via EV_{DNA}. In mice bearing orthotopic pancreatic ductal adenocarcinoma (PDAC) or glioblastoma (GBM), AT_{EVs} showed the highest accumulation in LNs, followed by tumor sites, 24h post i.v. injection (Figures 3A and S7A–S7D). While EVs derived from tumor cells are known for their homing efficacy to the originating tumor,[39,40] AT_{EVs} exhibited superior intratumoral distribution compared to either tumor cell-derived EVs or NT_{EVs}. In PDAC, T cell-derived EVs were predominantly taken up by tumor cells, FAP^+ tumor-associated fibroblasts, and endothelial cells, with <2% uptake by immune infiltrates (Figures 3B and S7E). $CD45^+$ immune cells internalizing AT_{EVs} were primarily antigen-presenting cells: $CD11c^+CD11b^-$ DCs (~35%), $CD11b^+$ myeloid cells (22%), and $B220^+$ B cells (13.5%), with the remainder comprising $CD3^+$ T (~23%) and NK (10%) cells (Figure S7F).

Notably, both NT_{EVs} and AT_{EVs} preferentially homed to LNs (Figures S1C and S1D) and tumor tissues compared to non-T cell EVs (Figures S7A and S7B). Proteomics identified the enrichment of the adhesion molecules ITGAL, ITGB2, and FGB in T cell- versus PDAC- or 3T3-derived EVs (Figure 3C). The integrin complex ITGAL-ITGB2 (LFA-1) and fibrinogen (FGB) bind ICAM1, an inducible cell adhesion molecule that is highly expressed in lymphoid tissues and upregulated in tumors,[41] but absent from most other normal tissues, including the brain, heart, lung, bone marrow, and liver in normal physiology.[42] Consistent with this, ICAM1 blockade in recipient mice significantly reduced AT_{EV} accumulation in LNs, spleen, and tumors, without affecting distribution to other organs (Figures 3D, 3E, S7G, and S7H), indicating ICAM1-dependent homing of AT_{EVs}.

PDAC is immunologically heterogeneous and typically poorly infiltrated by T cells.[43] A YFP^+ PDAC clone library from KPCY (*Kras*$^{LSL\text{-}G12D/+}$; *Trp53*$^{LSL\text{-}R172H/+}$; *Pdx1-Cre*; *Rosa26*$^{YFP/YFP}$) mice was previously established to generate tumors with either high or low T cell infiltration.[44] GSEA revealed APP pathway enrichment in tumor cells capable of eliciting high intra-tumoral T cell infiltration (KPCY-T^{hi}), relative to those from tumors with low T cell infiltration (KPCY-T^{lo}) (Figure S7I). Despite similar proliferation rates and EV particle or protein production across clones *in vitro*, KPCY-T^{hi} cells secreted significantly more EV_{DNA} than KPCY-T^{lo} cells (Figure S7J). A similar pattern was observed in breast cancer cells isolated from spontaneous MMTV-PyMT mammary tumors selected for high (PyMT-T^{hi}) versus low T cell infiltration (PyMT-T^{lo}) (Figures S7K–S7M). Normalized EV_{DNA} amounts from KPCY-T^{lo} and PyMT-T^{lo} cells resembled those from conventional tumor cell lines, whereas EV_{DNA} from KPCY-T^{hi} and PyMT-T^{hi} clones approached the levels observed in activated T cells (Figures S7J, S7M, and 2A). Consistently, freshly dissected primary tumor explants from patients with PDAC or glioma secreted EV_{DNA} amounts that positively correlated with the extent of intra-tumoral T cell infiltration (Figure S8), suggesting that T cell presence may increase tumor EV_{DNA} secretion.

To test whether these phenotypes were induced by AT_{EV} exposure and were EV_{DNA}-dependent, KPCY-T^{lo} cells were treated with PBS, NT_{EVs}, AT_{EVs}, or DNAse0-pretreated AT_{EVs} *in vitro*, followed by tumor EV characterization and transcriptomic analysis of the KPCY cells. AT_{EVs} elicited a dose-dependent upregulation of EV_{DNA} secretion from tumor cells (Figure S9A). 5 μg mL^{-1} of AT-EV_{DNA}, sufficient to significantly increase tumor cell-derived EV_{DNA}, was utilized for subsequent studies. Administration of PBS, NT_{EVs}, AT_{EVs}, or DNAse0-treated AT_{EVs} every other day over four weeks did not affect tumor cell morphology (Figure S9B), *in vitro* migration (Figures S9C–S9E), or proliferation (Figure S9F). However, AT_{EVs} significantly increased KPCY-T^{lo} secretion of EVs and EV_{DNA} by 2- and 4-fold, respectively, which was not observed by NT_{EVs} or DNAse0-treated AT_{EVs} (Figure S9F). Similar to the impact on DCs, AT_{EVs} drove the most pronounced and significant upregulation of APP-associated genes (Figures S9G and S9H) in tumor cells, unlike NT_{EVs} or DNAse0-treated AT_{EVs} (Figure 3F). Pathway enrichment analysis revealed that APP enrichment was specific to AT_{EV}-treated tumor cells, while other immunostimulatory pathways, including toll-like receptor (TLR) signaling, were enriched across multiple treatments (Figures S9I–S9K).

In vivo, KPCY-T^{lo} cells pre-treated with AT_{EVs} formed tumors that grew more slowly than PBS, NT_{EVs}, or DNAse0-treated AT_{EVs} controls after either subcutaneous (s.c.) or orthotopic (intrapancreatic) implantation. (Figures 3G, 3H, and S10). Tumors formed by AT_{EV}-educated cells showed increased infiltration of $CD8^+$ T cells, NK cells, and activated DCs, along with reduced infiltration of immunosuppressive $CD206^+$ macrophages and granulocyte-like myeloid-derived suppressor cells (G-MDSCs) (Figures 3I and S10A–S10P). Subcutaneous tumors also led to

(G) BrdU detection in EV_{DNA} and gDNA from non-activated and activated T cells by dot blot. T cells were pulsed ± BrdU for 12 h, then cultured in BrdU-free medium for 24 or 72 h; EV_{DNA} and gDNA were isolated at each time point post-medium refreshment. BrdU retention (%) was quantified relative to the 24h sample. Blot is representative of three independent biological replicates.

Significant differences measured using a one-way ANOVA with the Tukey test (A) and a two-tailed unpaired Student's *t* test (C, F). Data represent mean ± s.d. *p*-values are indicated.

See also Figures S4–S6, and Table S1.

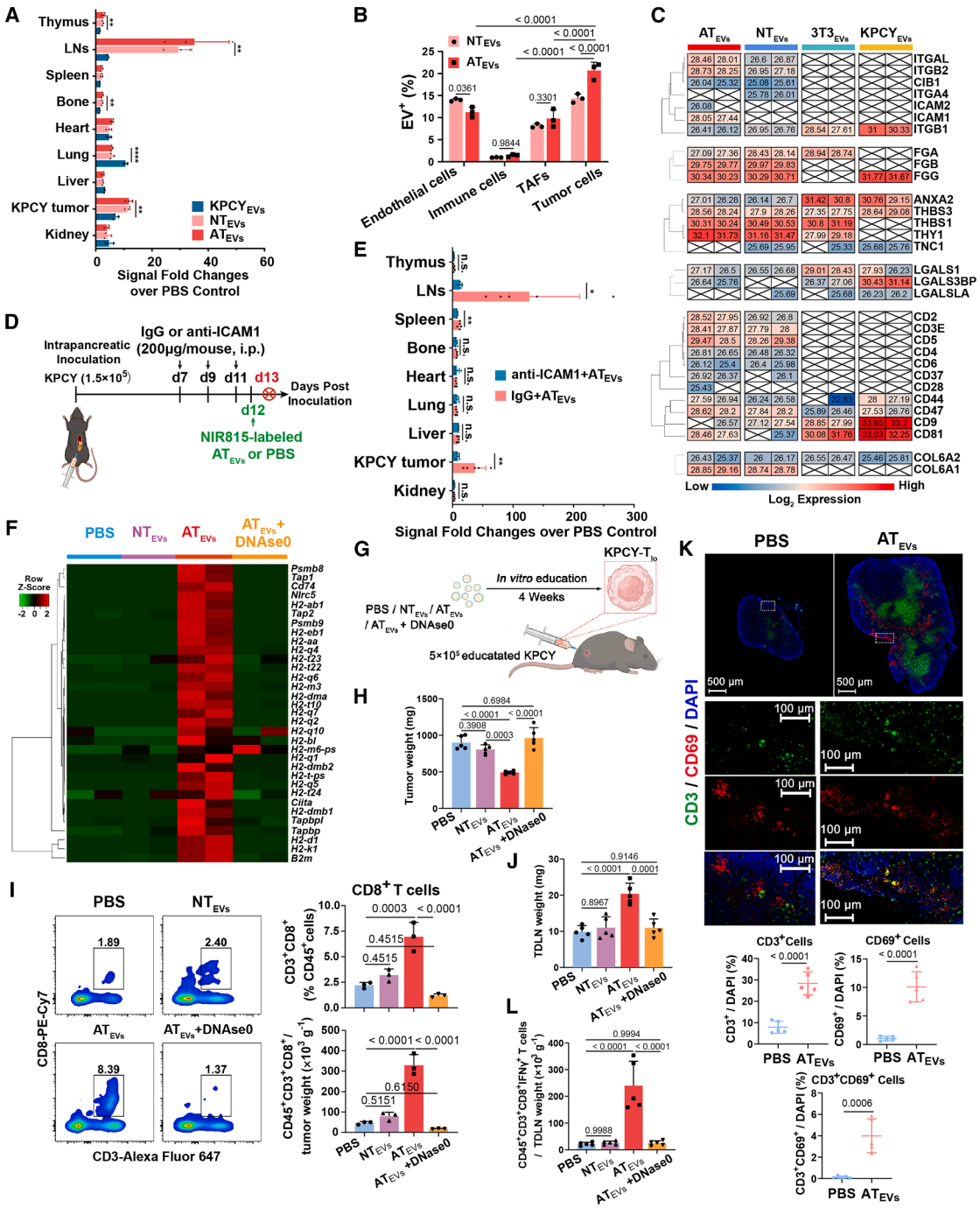

Figure 3. AT_{EVs} directly enhance the immunogenicity of tumor cells

(A) Fold-change analysis of NIR815-labeled EV biodistribution in mice bearing orthotopic PDAC (KPCY 6419c5) 24h after the retro-orbital i.v. injection of $KPCY_{EVs}$, NT_{EVs} or AT_{EVs}, quantified from whole-organ Odyssey images (Image Studio; normalized to the organ size). Signal fold changes were calculated by comparing experimental groups with PBS controls (n = 3 per group).

(B) Flow cytometric analysis of percentages of indicated cell subpopulations that uptake AT_{EVs} or NT_{EVs} in the tumor 24h after the retro-orbital injection of CellVue Burgundy-labeled T cell-derived EVs in orthotopic PDAC-bearing mice (n = 3 per group). Endothelial cells, FAP^-CD31^+; immune cells, $CD31^-FAP^-CD45^+$; TAFs, tumor-associated fibroblasts, $CD31^-FAP^+$; tumor cells, YFP^+.

(C) Heatmap of adhesion molecule abundance in AT_{EVs}, NT_{EVs}, $3T3_{EVs}$, and $KPCY_{EVs}$. Values represent log2-normalized protein abundance; crossed boxes, not detected.

(D) Schematic illustrating ICAM1 blockade followed by biodistribution analysis of NIR815-labeled AT_{EVs} in orthotopic PDAC-bearing mice.

(E) Fold-change analysis of NIR815-labeled EV biodistribution across organs 24h after the retro-orbital injection of AT_{EVs} in orthotopic PDAC-bearing mice pretreated with anti-ICAM1 or IgG control (n = 5 per group).

(legend continued on next page)

enlarged draining LNs with expanded T cell zones (Figures 3J and 3K) and elevated levels of IFNγ$^+$ CD8$^+$ (Figure 3L) and CD69$^+$ T cells (Figure 3K), consistent with enhanced tumor immunogenicity and antigen-specific T cell activation.

AT_{EVs} induce antitumor immunity in immunologically silent tumors *in vivo*

After confirming tumor-specific AT_{EV} uptake and its direct immunogenic effects on tumor cells, we next evaluated whether systemic AT_{EV} administration could overcome immune evasion and induce anti-tumor immunity. In an aggressive murine SB28 GBM model (intracranial injection of GFP$^+$ luciferase$^+$ SB28 cells with low to absent MHC-I expression[45]), mice received five i.v. doses of PBS, NT_{EVs}, or AT_{EVs} every three days, starting one week after tumor inoculation (Figure S11A). NT_{EVs} showed no anti-tumor efficacy, whereas AT_{EVs} halted tumor growth in 50% of mice after one week of treatment, significantly prolonging survival (Figures S11B–S11D). On Day 21 post-implantation, AT_{EVs} increased MHC-I expression on tumor cells and intratumoral DCs by 4-fold and induced MHC-II on tumor cells compared to PBS treatment (Figures S11E and S11F), driving robust infiltration of CD4$^+$ and CD8$^+$ T cells (∼7- and 20-fold increase, respectively), NK cells, and DCs (Figures S11G–S11J), while reducing immunosuppressive subsets (Figures S11K–S11M). Importantly, AT_{EV} treatment also induced the formation of tertiary lymphoid structures (TLSs), whose presence in tumors correlates with improved immunotherapy response (Figure S11N).[46]

In KPCY-T^{lo} PDAC s.c. model, intratumoral AT_{EVs} injections increased MHC-I expression on tumor cells, enhanced T and NK cell infiltration, and reduced G-MDSCs within tumors (Figures S12A–S12C). Despite changes in the immune microenvironment, AT_{EVs} only slightly slowed tumor growth (Figures S12D and S12E). Tumor bulk RNAseq revealed that several inhibitory checkpoints, including *Pd1/Pd-l1*, *Ctla4*, *Siglec5*, *Btla*, *Cd160*, *B7h4*,[47] were upregulated following AT_{EV} treatment (Figures S12F–S12I). To counteract this immunosuppressive adaptation, we combined AT_{EVs} with anti-PD1 ICI in the orthotopic model of luciferase-expressing PDAC (Figure 4A). Anti-PD1 alone had a minimal therapeutic effect due to poor T cell infiltration. Although AT_{EVs} extended median survival by ∼1 week, the combination synergistically suppressed tumor growth and significantly prolonged survival (Figures 4B, 4C, and S12J). While AT_{EVs} alone enhanced MHC-I expression on tumor cells and intratumoral DCs (Figure 4D), the combination significantly upregulated both MHC-I and MHC-II on tumor cells (Figure S12K). Similar to the GBM model, AT_{EVs} induced TLS formation, characterized by the presence of CD21$^+$ follicular DCs, B220$^+$ B cells, and CD3$^+$ T cells (Figure 4E). Compared to AT_{EVs} alone, the combination formed larger and more organized TLSs with significantly increased B and T cell presence (Figure 4F). Importantly, the combination treatment also reduced liver metastases (quantified by flow cytometry of YFP$^+$ KPCY cells) by 3-fold relative to PBS or anti-PD1 alone, despite similar primary tumor sizes at endpoint (approximately Day 25 for PBS and anti-PD1, Day 31 for the AT_{EVs}, and Day 45 for combination treatment) (Figure S12L).

In the orthotopic PyMT-T^{lo} breast cancer model (Figure 4G), treatments began at the onset of tumor exponential growth (Day 28 post-inoculation, Figure S12M). The combination treatment maximally reduced tumor burden and prolonged survival (Figures 4H and 4I). Both AT_{EVs} and the combination treatment significantly upregulated MHC-I/II on intratumoral DCs (Figures 4J and S12N) and CD45$^-$CD31$^-$FAP$^-$ tumor cells (Figures 4K and S12O), enhanced intra-tumoral infiltration of CD4$^+$ and CD8$^+$ T cells (Figure 4L), activated DCs, NK cells, and reduced CD206$^+$ macrophages and G-MDSCs (Figures S12P-S12S). Compared with AT_{EVs} alone, the combination further boosted CD8$^+$ T cell infiltration and DC activation (Figure 4L). Similar to the PDAC model, AT_{EV} treatment significantly increased PD1 expression on CD4$^+$ and CD8$^+$ T cells (Figures S12T and S12U), which was reversed by the addition of anti-PD1. Notably, AT_{EV} monotherapy was most effective in the SB28 model (Figures S11C, S11D, 4B, 4C, 4H, and 4I), potentially due to tumor-intrinsic MHC differences: While MHC-I is expressed on both KPCY and PyMT cells, it is absent on SB28 cells (Figure S12V), rendering them more responsive to AT_{EV} treatment. Taken together, our data demonstrate that AT_{EVs} enhance APP in tumor cells and DCs across multiple immunologically cold tumors, and synergize with ICIs to elicit anti-tumor immunity and restrain tumor growth.

AT_{EV}-induced APP upregulation can occur independently of IFN-γ and cytosolic DNA sensors

To explore how AT_{EVs} upregulate APP pathways, we first examined known drivers of antigenicity. IFN-γ is the most potent inducer of MHC-I/II via JAK-STAT1-IRF1 signaling,[48–50] and IFN-γ signaling was the top-enriched pathway in AT_{EV}-educated DCs and tumor cells (Figures S2I and S9I). While undetectable in

(F) Heatmap of APP-associated gene expression in 6415c5 cells after treatment with PBS, NT_{EVs}, AT_{EVs} with or without DNAse0 pretreatment. Normalized mRNA expression is row-wise z-scored.
(G) *Ex vivo* tumor 'education' schematics for the s.c. PDAC model. 6419c5 cells were treated with PBS, NT_{EVs} or AT_{EVs} (containing 5 μg mL^{-1} EV_{DNA}), or DNAse0-pretreated AT_{EVs} every other day for 4 weeks, then 5×10^5 6419c5 cells were subcutaneously inoculated into syngeneic mice.
(H) Weights of dissected s.c. tumors (from G) on Day 22 after inoculation (n = 5 per group).
(I) Representative flow cytometric plots (left) and percentages (right) among CD45$^+$ cells and cell numbers for CD8$^+$ T cells in s.c. tumors from G (n = 3 per group).
(J) Weights of tumor-draining lymph nodes (TDLNs) on Day 22 after s.c. tumor inoculation (n = 5 per group).
(K) Immunofluorescence staining of CD3 and CD69 in TDLNs from mice bearing PBS and AT_{EV}-treated s.c. tumors. White boxed regions are shown at higher magnification to highlight the spatial localization of CD3$^+$ and CD69$^+$ T cells. Scale bars, 500 μm (overview) and 100μm (magnified). CD3$^+$, CD69$^+$, and CD3$^+$CD69$^+$ cells were quantified per TDLN by ImageJ (n = 5 per group).
(L) Flow cytometric analysis of IFNγ$^+$CD8$^+$ T cell numbers in TDLNs of mice bearing PBS and AT_{EV}-treated tumors (n = 5 per group).
Significant differences measured using a one-way ANOVA with Tukey test (A, H-J, L), and a two-tailed unpaired Student's t test (B, E, K). Data represent mean ± s.d. *p < 0.05, **p < 0.01, and ****p < 0.0001, n.s., not significant, or p-values are indicated.
See also Figures S7–S10.

CellPress
OPEN ACCESS

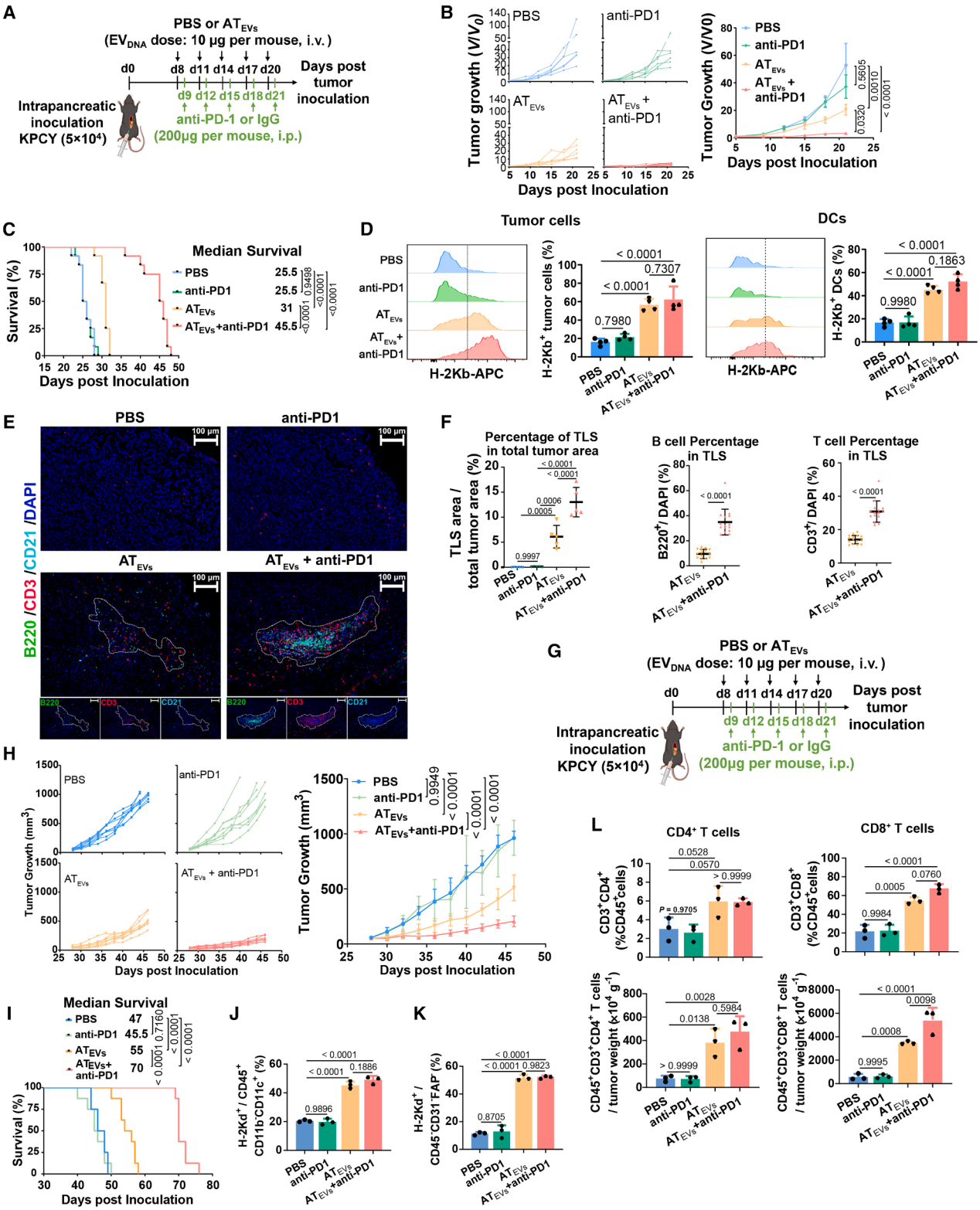

Figure 4. AT_{EVs} induce antitumor immunity in immunologically silent tumors *in vivo*

(A) Schematic of orthotopic 6419c5 PDAC inoculation and treatment with PBS, AT_{EVs}, anti-PD1, or AT_{EVs} + anti-PD1.

(B) PDAC growth profiles, quantified as fold-change from baseline (*V/V0*) by bioluminescence (*n* = 6 per group).

(C) Kaplan-Meier survival of 6419c5 PDAC-bearing mice (*n* = 12 per group).

(legend continued on next page)

NT_{EVs}, ~4ng of IFN-γ was found in 1 mg of AT_{EVs} (Figure S13A). We therefore explored the potential impact of AT_{EV}-associated IFN-γ. In DC2.4 cells, the inhibition of the Janus kinases (JAK) responsible for IFN signal transduction with a pan-JAK inhibitor (SAR-20347, JAKi) reduced IFN-γ (5ng/mL)-induced MHC-I expression by >60% and abolished MHC-II upregulation (Figure S13B). However, in AT_{EV}-treated DC2.4 cells (AT_{EVs} contain <0.1ng/mL of IFN-γ), JAKi only slightly reduced AT_{EV}-elicited MHC-I/II upregulation, whereas DNAse0 completely eliminated AT_{EV}-induced MHC and APP gene upregulation (Figures 5A and S13C). Thus, AT_{EV}-associated DNA may drive APP machinery upregulation in recipient cells through mechanisms other than IFN-γ signaling.

Since IL-2 is present in activated but not non-activated T cell cultures, we tested its association with AT_{EVs} and potential contribution to APP upregulation in DCs. IL-2 levels did not differ between NT_{EVs} and AT_{EVs}, and EV-depleted AT conditioned medium contained ~30-fold more IL-2 than AT_{EVs} (Figure S13D), indicating that IL-2 is primarily non-EV-associated. Minimal IL-2 association with EVs was also confirmed in NT cultures supplemented with IL-2. As expected, only $AT_{Evs,}$ but not NT_{EVs} or IL-2-supplemented NT_{EVs} (NT_{EV}+IL-2) led to MHC-I upregulation in DC2.4 cells (Figure S13E). Therefore, IL-2 is not responsible for AT_{EV}-mediated DC activation.

Cyclic GMP-AMP synthase (cGAS), TLR9, and absent in melanoma 2 (AIM2) are key cytosolic DNA sensors that trigger type I/II IFNs and other pro-inflammatory signaling upon activation.[51–54] Given the critical role of EV_{DNA} in AT_{EV}-induced immunogenicity, we explored whether AT-EV_{DNA} stimulates intracellular DNA sensors, which subsequently activate IFN pathways and APP machinery. In BlaER1 monocytes, AT_{EVs} and agonists for cGAS (G3-YSD) and AIM2 (Poly (dA:dT)) upregulated both MHC-I (HLA-A, B, C) and MHC-II (HLA-DR, DP, DQ), whereas CpG (TLR9 agonist) had no effect (Figure 5B), likely due to low baseline TLR9 expression. The pan-DNA sensor antagonist (A151) blocked G3-YSD or Poly (dA:dT)-induced HLA upregulation but did not affect AT_{EV}-mediated HLA upregulation. In the stimulator of IFN genes (*STING*) knockout BlaER1, while G3-YSD failed to upregulate HLA molecules, AT_{EVs} remained effective (Figure 5C). Additionally, phosphorylation of STING and TBK1, hallmarks of cGAS signaling,[55] was not detected in AT_{EV}-treated DC2.4 (Figure 5D). In DC2.4 cells, while A151 blocked both CpG- and Poly (dA:dT)-induced MHC upregulation, it did not affect AT_{EV}-dependent MHC-I/II upregulation (Figure S13F). Collectively, these data suggest mechanisms distinct from DNA sensor activation contribute to AT_{EV}-induced immunogenicity.

EV_{DNA}-mediated horizontal gene transfer drives transient AT_{EV}-induced antigenicity

Since AT_{EVs} carry higher copy numbers of genes within EV_{DNA}, many of which are upregulated in AT_{EV}-treated recipient cells in a DNA-dependent manner (Figure S4M), we tested whether direct transfer of APP-enriched EV_{DNA} enhances tumor antigenicity. Cross-species treatment of human 293T cells with mouse AT_{EVs} significantly upregulated mouse, but not human, APP genes (Figure S14A), supporting functional gene transfer. Next, we evaluated the potential of AT_{EVs} to restore APP in MHC-I/II double knockout (DKO) BMDCs (Figure 6A). AT_{EVs} from wild-type mice reinstated MHC-I/II expression in ~30% of MHC-deficient BMDCs within 24h, whereas LPS alone failed to activate these cells (Figure 6B). Moreover, APP function was rescued in ovalbumin (OVA)-pulsed MHC I/II-DKO BMDCs pre-treated with AT_{EVs}, promoting T cell proliferation and expansion of OVA-specific $CD8^+$ T cells (Figures 6C and 6D). *In vivo*, BALB/c AT_{EVs} (H-2Kd MHC-I haplotype) induced donor H-2Kd expression on C57BL/6 LN-DCs, in addition to endogenous H-2Kb induction (Figures 6E and S14B). Reciprocally, C57BL/6 AT_{EVs} induced H-2Kb, rather than H-2Kd expression in BALB/c mice. Similar results were observed *in vitro* upon the cross-education of 4T1 cells (breast tumor cells from BALB/c mice) with C57BL/6 AT_{EVs} or SB28 cells (GBM cells from C57BL/6 mice) with BALB/c AT_{EVs} (Figures S14C–S14E).

As transcription requires EV_{DNA} delivery to the nucleus, we stained EV_{DNA} using a cell-impermeable fluorescent dye and tracked its localization in live KPCY and DC2.4 cells. As expected, AT_{EV}-associated DNA predominantly localized to euchromatic (Hoechst-dim) regions of the nucleus, whereas NT_{EV}-associated DNA remained perinuclear in the cytosol (Figures 7A and S15A). Notably, AT-EV_{DNA} fluorescence did not co-localize with heterochromatic areas of the nucleus, but only the euchromatic regions, which represent transcriptionally active regions of chromatin.

We next tested whether AT-EV_{DNA} transfer to recipient cells is sufficient for donor MHC expression. Purified mouse AT-EV_{DNA} delivered by lipofectamine ($^{mAT}EV_{DNA}$/Lipo) was sufficient for murine APP gene expression in 293T cells, which was diminished when DNA was extracted from DNAse0-treated AT_{EVs} (Figure 7B). Despite EV_{RNA} level being substantially lower than EV_{DNA} (Figure S4E), we evaluated the potential role of EV_{RNA}-

(D) Flow cytometry detection of H-$2K^b$ on YFP^+ tumor cells and tumor DCs on day 23 after inoculation (n = 4 per group).
(E) Immunofluorescence staining of anti-CD3, anti-B220, and anti-CD21 of intratumoral tertiary lymphoid structures (TLS, within dashed lines) in dissected PDAC tumors on Day 23 after inoculation. Scale bars, 100 μm.
(F) TLS area (% total tumor area) quantified by ImageJ across treatment groups. Percentages of $CD3^+$ T cells and $B220^+$ B cells in the TLS of AT_{EVs} or AT_{EVs}+anti-PD1 treated tumors were quantified in three randomly selected TLS per sample by ImageJ (n = 5 tumors per group).
(G) Schematic of orthotopic PyMT-T^{lo} breast tumor inoculation and treatment with PBS, AT_{EVs}, anti-PD1, or AT_{EVs} + anti-PD1.
(H) PyMT growth profiles (n = 8 per group).
(I) Kaplan-Meier survival of PyMT tumor-bearing mice (n = 8 per group).
(J, K) Flow cytometry detection of H-$2K^d$ (MHC class I) on tumor DCs (J) or $CD45^-CD31^-FAP^-$ cells (mainly tumor cells, K) on day 36 after inoculation (n = 3 per group).
(L) Flow cytometric analysis of intratumoral $CD4^+$ and $CD8^+$ T cell frequencies (of $CD45^+$ cells) and cell numbers on day 36 after inoculation (n = 3 per group).
Significant differences measured using a two-way ANOVA with multiple comparisons (B, H), a log-rank test (C, I), a one-way ANOVA with Tukey test (D, F (TLS percentages), J-L), and a two-tailed unpaired Student's t test (F (B and T cell percentages)). Data represent mean ± s.d. p-values are indicated.
See also Figures S11 and S12.

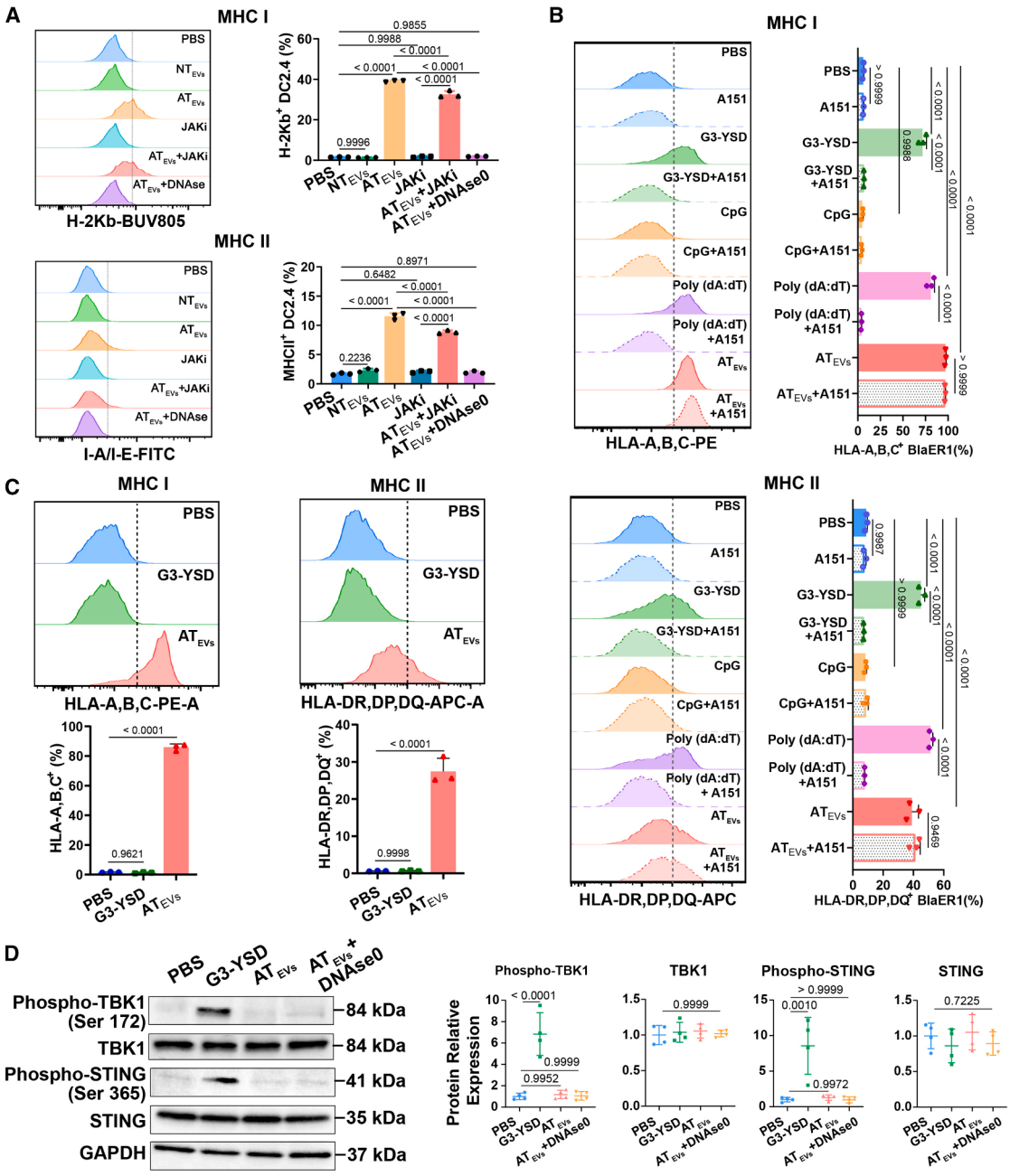

Figure 5. IFN-γ and cytosolic DNA sensing contribute to the upregulation of antigen presentation machinery by AT_{EVs}

(A) Flow cytometry analysis of H-2K^b and I-A/I-E on DC2.4 cells treated with PBS, NT_{EVs} or AT_{EVs} (containing 5 μg mL^{-1} EV_{DNA}), SAR-20347 (JAKi, 2μM), AT_{EVs} combined with JAKi, AT_{EVs} pretreated with DNAse0 (n = 3).

(B) Flow cytometry analysis of HLA expressions on BlaER1-derived monocytes treated with PBS, A151 (2 μM), G3-YSD (5 μg mL^{-1}), CpG ODN 2006 (1 μM), Poly (dA:dT) (5 μg mL^{-1}), AT_{EVs} (containing 5 μg mL^{-1} of EV_{DNA}), or A151 combined with G3-YSD, CpG, Poly (dA:dT) or AT_{EVs} (n = 3).

(C) Flow cytometry analysis of HLA on STING-knockout BlaER1 monocytes treated with PBS, G3-YSD (5 μg mL^{-1}), or AT_{EVs} (5 μg mL^{-1} of EV_{DNA}) (n = 3).

(D) Western blot analysis of TBK1, STING, and their phosphorylation. Loading control: GAPDH. Data are representative of four independent experiments. Cumulative densitometric analysis of western blotting images was performed by ImageJ (n = 4).

Significant differences measured using a one-way ANOVA with the Tukey test (A-D). Data represent mean ± s.d. p-values are indicated.

See also Figure S13.

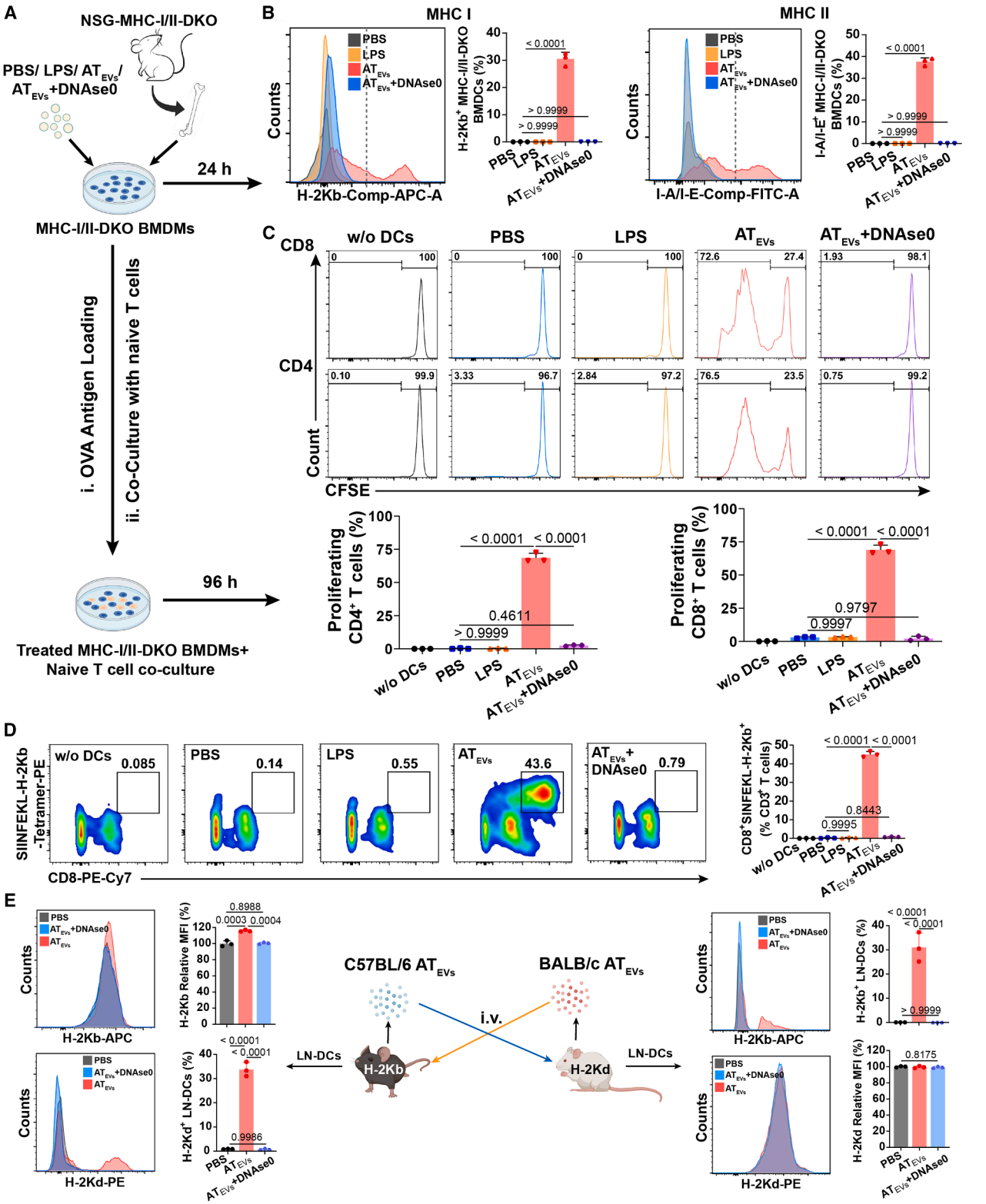

Figure 6. AT_{EVs} boost immunogenicity via transient horizontal EV_{DNA} transfer

(A) Workflow of BMDM treatments from NSG-MHC-I/II-DKO mice and subsequent model antigen loading and co-culture with naive T cells.

(B) Flow cytometry analysis of H-2K^b and I-A/I-E on MHC-I/II-DKO BMDCs treated with PBS, LPS, AT_{EVs}, and DNAse0-pretreated AT_{EVs} (n = 3 mice).

(legend continued on next page)

mediated transfer of APP genes. *H2-k1* mRNA was undetectable in AT_{EVs}, and the mRNA cargo representing other APP-related genes was similar between NT_{EVs} and AT_{EVs} (Figure S15B). Given that APP gene expression upregulation occurred exclusively in cells treated with AT_{EVs}, but not with NT_{EVs}, EV_{RNA} transfer is unlikely to drive this effect. Furthermore, murine APP genes were upregulated in 293T cells by $^{mAT}EV_{DNA}$/Lipo but not by AT-EV_{RNA} complexed with lipofectamine ($^{mAT}EV_{RNA}$/Lipo) (Figure S15C).

Beyond direct upregulation of APP-associated genes, we tested whether AT_{EVs} promote immunogenicity by inducing pro-inflammatory cytokines in recipient cells, and whether these effects are EV_{DNA}-dependent. By examining cytokine gene expression in LN-DCs from mice treated with PBS, NT_{EVs}, AT_{EVs}, or DNAse0-pretreated AT_{EVs}, we found AT_{EVs} significantly upregulated multiple cytokines and chemokines, including *Il2, Il21, Il1a, Il12b, Cxcl5, Cxcl13, Cxcl2, Cxcl12, Cxcl1, Ccl6, Ccl11, Ccl2, Ccl7, Ccl21a*, and *Ifng* (Figure S15D), relative to PBS. While APP gene upregulation was strictly EV_{DNA}-dependent (Figure S2F), the expression of most cytokines was only partially AT-EV_{DNA}-dependent, remaining largely unchanged by DNAse0 + AT_{EVs}. *Ccl6*, *Cxcl2*, and *Ifng* were induced by AT_{EV} in an EV_{DNA}-dependent manner, but only *Ifng* was exclusively upregulated by AT_{EVs}, whereas *Ccl6* and *Cxcl2* were also induced by NT_{EVs} (Figure S15E), suggesting that IFN-γ induction may serve as an indirect EV_{DNA}-dependent mechanism underlying AT_{EV}-driven anti-tumor immunity. *Ifng* enrichment in AT_{EV}-DNA (Figure 2E) raises the possibility that IFN-γ itself may be induced through EV_{DNA} transfer. Since IFN-γ is known to promote APP, this AT_{EV}-DNA-induced IFN-γ likely amplifies DC antigen presentation and cross-presentation alongside direct APP gene transfer. This is further supported by the slight reduction in AT_{EV}-induced MHC upregulation with JAK inhibition (Figure 5A). IL-21, a cytokine enhancing intratumoral lymphocyte infiltration and pro-inflammatory T cell activation,[56,57] was also uniquely induced by AT_{EVs}, and likely dependent on EV_{DNA}, as indicated by a clear reduction trend following DNAse0 treatment.

To uncover how EV_{DNA} enters the nucleus, we compared protein cargo between NT_{EVs} and AT_{EVs} via unbiased proteomics and identified granzyme B (Gzmb) as the top AT_{EV}-enriched protein (Figure 7C), present regardless of T cell activation method but absent in NT_{EVs} and BMDC-derived EVs (Figure S16A). Consistent with Gzmb-mediated lamin cleavage and nuclear envelope integrity disruption,[58,59] AT_{EVs}, but not NT_{EVs} caused nuclear GFP leakage into the cytoplasm in 4T1 cells expressing nuclear-localized GFP (NLS-GFP) (Figure 7D),[60] The leakage was blocked by pre-treatment of AT_{EVs} with Gzmb inhibitor IV (Gzmbi), which inhibited AT_{EV}-associated Gzmb activity by 95% (Figure S16B). In DC2.4 DCs, Gzmbi reduced AT-EV_{DNA} nuclear localization (Figure 7A), abolished MHC-II induction, and reduced MHC-I expression by 85% (Figure 7E). Therefore, AT_{EV}-induced immunogenicity requires Gzmb-mediated EV_{DNA} access to the nucleus.

Given AT_{EV}-enabled EV_{DNA} nuclear access, we investigated whether EV_{DNA} integrates into the host genome, achieving sustained APP upregulation. gDNA from PBS- or AT_{EV}-treated BMDCs was analyzed by nanopore long-read sequencing, which sensitively detects genomic insertions.[61] As a positive control, lentiviral transduction yielded detectable viral integration in 18% of sequenced reads (Figures S16C). To exclude adapter sequences and other nonspecific short fragments, only read ends >50 bp were analyzed (Figure S16D). Of the 7829 reads sequenced, 1437 viral molecules contained unique ends not observed among read ends aligned to the viral reference in the PBS condition, which represent background signal. In contrast, APP-related genes were detected at similarly low frequencies (0–7%, representing the background noise threshold) in both AT_{EV}^{-} or lentiviral control-treated groups relative to PBS treatment (Figures S16C), indicating no detectable donor APP gene integration following AT_{EV} treatment. Consistent with this finding, donor H-2Kd induction by BALB/c AT_{EVs} in recipient C57BL/6 DC2.4 cells was transient, with a marked reduction by day 3 post-treatment and complete loss by day 7 (Figure S16E).

Together, these data support a model in which AT_{EVs} act as natural, transient transfection vehicles: Gzmb disrupts the nuclear envelope to enable EV_{DNA} nuclear entry, driving the expression of specific genes (e.g., APP) enriched in EV_{DNA}, while cytokine induction further amplifies downstream anti-tumor immunity.

DISCUSSION

Our work reveals an EV-mediated mechanism through which activated T cells enhance APP across diverse recipient cells - from DCs in physiological conditions to cancer cells across tumor types. Specifically, AT_{EVs} deliver genomic EV_{DNA} enriched in APP and immune-related genes into recipient cell nuclei through Gzmb-mediated nuclear entry, enabling transient transcription of immunogenic genes. By boosting APP machinery, AT_{EVs} enhance tumor immunogenicity and elicit robust anti-tumor responses, particularly when combined with ICIs in otherwise resistant tumors, including pancreatic, breast, and brain cancers.

The tropism of T cell-derived EVs for lymphoid tissues and tumors highlights their potential as an acellular immunotherapy, as well as a targeted delivery vehicle for vaccines and anti-tumor agents. This tissue specificity is presumably mediated by cell adhesion molecules, such as selectins and integrins.[62,63] Herein, we identified ICAM-1 as a key host receptor facilitating AT_{EV} accumulation in LNs and tumors. Further validation of adhesion

(C) Activation of naive C57BL/6 $CD8^+$ and $CD4^+$ T cells by OVA-pulsed MHC I/II-DKO BMDCs following treatments in (B). T cell proliferation was measured by CFSE dilution. Upper: representative histograms. Bottom: cumulative data (n = 3).
(D) Flow cytometry analysis of OVA-specific $CD8^+$ T cells following activation in (C) (n = 3).
(E) *In vivo* cross-strain education and flow cytometry of H-$2K^b$ and H-$2K^d$ on LN-DCs. C57BL/6 (or BALB/c) mice were injected retro-orbitally with 10 μg of AT_{EVs} isolated from BALB/c (or C57BL/6) mice, with or without DNAse0 pretreatment. 24h post-injection, cervical LNs were isolated, and MHC class I haplotypes on DCs in each treatment group were measured (n = 3). MFI, median fluorescence intensity.
Significant differences were measured using a one-way ANOVA with the Tukey test (B-E). Data represent mean ± s.d. p-values are indicated.
See also Figure S14.

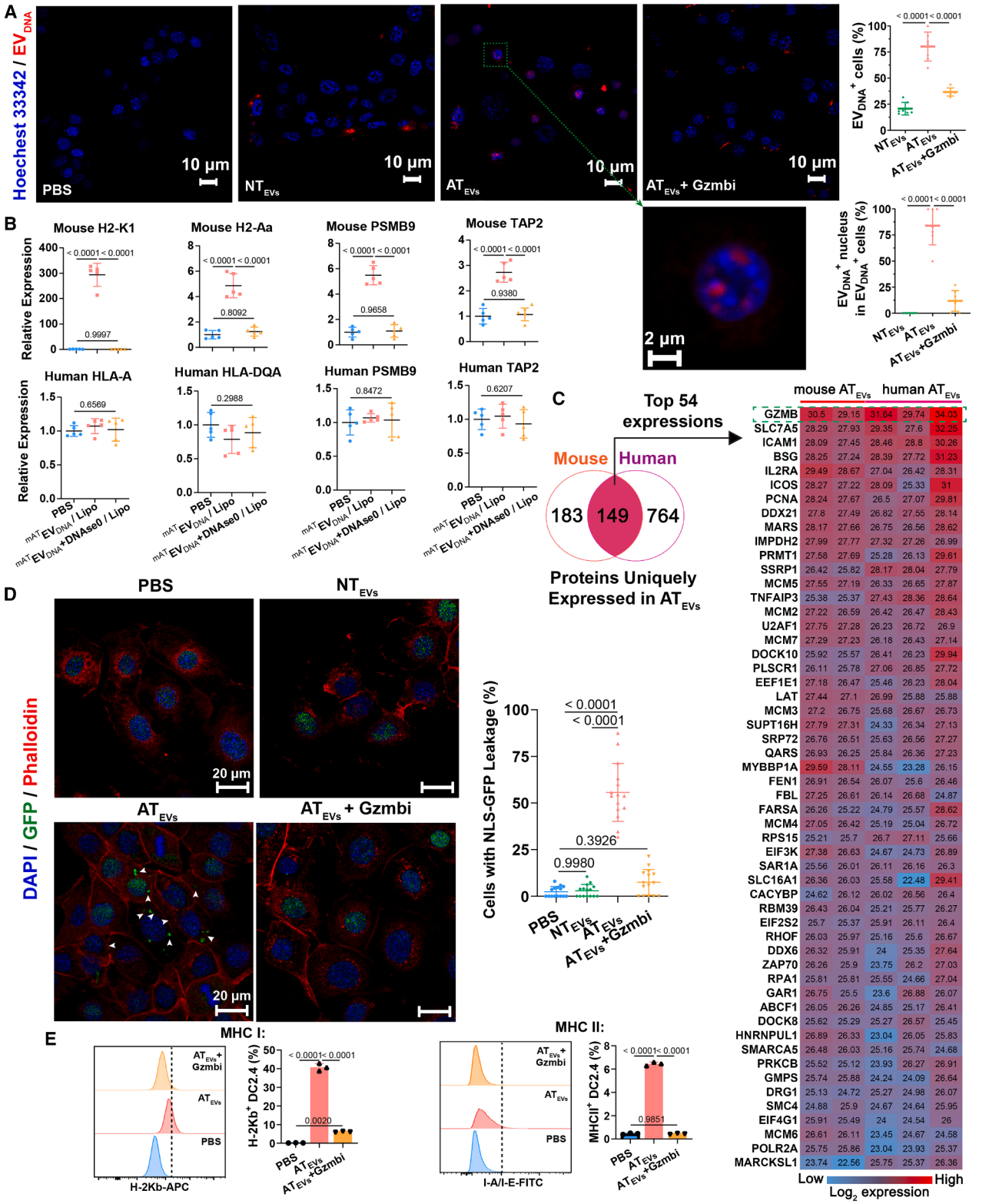

Figure 7. AT_{EV}-associated granzyme B facilitates nuclear entry of EV_{DNA}

(A) Localization of TOTO-3 Iodide-labeled EV_{DNA} within recipient 6419c5 cells stained with Hoechst 33342 following 6h incubation with NT_{EVs}, AT_{EVs}, or AT_{EVs} pretreated with Gzmb inhibitor IV (Gzmbi, 5 μM). Scale bars, 10 μm and 2 μm for magnified images. The fraction of recipient tumor cells with intracellular EV_{DNA} and the fraction of EV_{DNA}^+ recipient tumor cells with intranuclear EV_{DNA} were quantified in three or four randomly selected fields per sample using ImageJ ($n = 2$).

(legend continued on next page)

molecules on AT_{EVs} (e.g., ITGB2/ITGAL or LFA-1) may guide the development of biomimetic delivery platforms that replicate T cell EV targeting.

EV_{DNA} remains underexplored as a functional cargo. Prior studies attribute EV_{DNA}-induced immune activation to cytosolic DNA sensing, particularly via the cGAS-STING pathway.[64,65] However, our findings suggest minimal cGAS-STING involvement, potentially because T cell EV_{DNA} is chromatinized, limiting cGAS access,[66] oligomerization, and activation.[67,68] This aligns with a recent study showing that EV_{DNA}-induced cGAS-STING activation is induced by unchromatinized DNA fractions originating from mitochondria,[64] which is only detected at very low levels in AT-EV_{DNA} (<0.01%). Instead, AT-EV_{DNA} may promote anti-tumor immunity both by directly upregulating APP genes in recipient cells and by enhancing EV_{DNA} release from tumor cells. The latter mechanism can trigger DNA damage responses in innate immune cells, driving pro-inflammatory cytokine production and TLS formation in pre-metastatic niches.[24]

Our findings also reveal AT_{EVs}' function in mediating horizontal gene transfer. Nuclear entry remains a major hurdle for non-viral DNA therapeutics.[69] The barrier has led to a shift toward the development of mRNA therapeutics, albeit less stable and more costly.[70,71] AT_{EV}-associated Gzmb-enabled nuclear delivery of EV_{DNA} suggests a blueprint for improved non-viral DNA delivery. Our findings support intranuclear translocation and subsequent expression of AT-EV_{DNA}. The presence of promoter regions within APP-associated genes in AT-EV_{DNA} and the transient nature of donor MHC induction in recipient cells support episomal transcription without genomic integration. Since AT-EV_{DNA}-mediated activation of APCs is likely a mechanism evolved to amplify physiological immune responses to pathogens, the transient expression is beneficial to limit autoimmunity. However, the mechanisms of episomal transcription and engagement of host transcriptional machinery remain to be defined.

Extracellular DNA originates from both cellular death and active secretion.[72] Our T cell viability data indicate that T cell EV_{DNA} is not the result of cell death. Instead, pulse-chase experiments revealed that newly synthesized DNA is a primary source of AT-EV_{DNA}, aligning with previous reports indicating that mitogen-stimulated lymphocytes release newly synthesized DNA extracellularly.[73] Future studies will determine how newly synthesized DNA is exported, packaged into EVs, and selectively enriched for APP genes. Mechanistic insight could enable therapeutic tuning of T cell EV_{DNA} release, either enhancing it to promote immune responses in cancer or infection, or reducing it to attenuate T cell-mediated inflammation in autoimmunity.

Overall, AT_{EVs} emerge as an acellular immunotherapy and delivery modality that can prime antitumor immunity, synergize with existing therapies, and serve as a vaccine adjuvant. This strategy may address diseases characterized by insufficient immune surveillance, including but not limited to immune-silent tumors. Our findings provide a foundation for the therapeutic application of AT_{EVs} through a deeper understanding of the biological role of AT-EV_{DNA}.

Limitations of the study

The study uses pan T cell-derived EVs for mechanistic and functional studies. Whether the EVs and EV_{DNA} from helper and cytotoxic T cells cooperate to boost immunogenicity remains to be determined. The cellular mechanisms driving increased EV_{DNA} secretion and the enrichment in specific genes packaged into T cell EVs upon activation, particularly those associated with APP and immune responses, also require further study. Finally, AT_{EV} dosing parameters, such as intervals and treatment duration, need to be optimized across tumor models to maximize antitumor efficacy and support clinical translation.

RESOURCE AVAILABILITY

Lead contact

Further information and requests for resources should be directed to and will be fulfilled by the Lead Contact, David Lyden (dcl2001@med.cornell.edu).

Materials availability

All unique reagents generated in this study are available upon request from the lead contact with a completed materials transfer agreement.

Data and code availability

Raw RNAseq have been deposited into the Gene Expression Omnibus under accession codes GSE290812, GSE290972, GSE291466, and GSE325678. WGS data have been deposited into the NIH BioProject under accession codes PRJNA1135491 and PRJNA1231632. Nanopore long-read raw and basecalled data have been deposited into the European Nucleotide Archive under accession code PRJEB83979. Scripts related to the Nanopore long-read DNA-sequencing analysis have been deposited at: https://github.com/Theo-Nelson/evdna-integration. Proteomics data have been deposited to the ProteomeXchange Consortium via the PRIDE partner repository[74] with the dataset identifiers PXD075986 and PXD075814. Any additional information required to reanalyze the data reported in this paper is available from the lead contact upon request.

ACKNOWLEDGMENTS

We thank the Genomics Resource Core Facility (Weill Cornell Medicine (WCM)), New York Genome Center, Electron Microscopy and Histology Core Facility (WCM), Flow Cytometry Core Facility (WCM), Optical Microscopy Core (WCM), Proteomics Resource Center (the Rockefeller University), Tumor Assessment Core and Molecular Cytogenetics Core (Memorial Sloan Kettering Cancer Center (MSKCC)) for their high-quality service. We appreciate the help of Dr. Alexander Rudensky (MSKCC) for providing reagents during the revision. Moreover, we acknowledge members of the Lyden and Pascual

(B) Q-PCR of murine and human MHC and APP-associated genes in 293T cells treated with PBS, lipofectamine 3000 (Lipo)-mediated transfection of mouse AT-EV_{DNA} ($^{mAT}EV_{DNA}$) or DNAse0-pretreated $^{mAT}EV_{DNA}$ (n = 5).
(C) Heatmap of the 54 most abundant AT_{EV}-specific proteins shared between mouse and human activated T cell EVs.
(D) Representative images of NLS-GFP expressing 4T1 cells after 6 h of treatment with PBS, NT_{EVs}, AT_{EVs}, or AT_{EVs} pretreated with Gzmbi (5 μM), labeled with phalloidin and DAPI. Scale bars, 20 μm. The frequency of cells with cytoplasmic GFP signal was quantified in five randomly selected fields per sample using ImageJ (n = 3).
(E) Flow cytometry analysis of H-$2K^b$ and I-A/I-E expression on DC2.4 cells treated with PBS and AT_{EVs} ± Gzmbi (5 μM) (n = 3).
Significant differences were measured using a one-way ANOVA with the Tukey test (A, B, D, E). Data represent mean ± s.d. p-values are indicated.
See also Figures S15 and S16.

laboratories, Michel Sadelain, and Leaf Huang for insightful scientific discussions. Schematics were generated using BioRender (https://www.biorender.com/).

This work was supported by CTSC-TL1 training award (2TL1-TR-2386 to M.H.), grants from the NCI (CA232093 to D.L.), the NIAID (ACE U19 AI144301 to D.L. and V.P.), the Pershing Square Sohn Foundation (to D.L.), the Thompson Family Foundation (to D.L. and D.K.), the Tortolani Foundation (to D.L. and J.Br.), the Theodore A. Rapp Foundation, the Pediatric Oncology Experimental Therapeutics Investigator's Consortium, the Malcolm Hewitt Weiner Foundation, the Manning Foundation, the Sohn Conference Foundation, the AHEPA Vth District Cancer Research Foundation, the Children's Cancer and Blood Foundation, the Hartwell Foundation (to D.L. and J.Bu.), the Fonds De La Recherche Scientifique Excellence of Science grant 40007532 (A.N., G.B., D.L.). T.M.N. was supported by a Medical Scientist Training Program grant (NIGMS T32GM152349).

AUTHOR CONTRIBUTIONS

D.L., I.R.M., H.Z., and M.H. were responsible for the conception of the study. M.H. designed the experimental approach, performed most of the experiments, analyzed and interpreted the data, and wrote the manuscript. D.A.L. performed substantial experiments and interpreted data. I.R.M. and H.Z. designed the experimental approach. P.C., T.M.N., J.F., G.Z., and H.S.K. processed and analyzed nanopore sequencing data and WGS data. L.B. coordinated the patient sample preparation and documentation. D.K. and W.R.J. provided human samples. I.W., G.T., T.A., C.M.K., G.W., Z.W., S.Q., R.P., P.R., J.A.B, S.X, H.W., P.L., and H.M. performed experiments. S.C. provided wild-type and STING-KO BlaER1 cells and provided help with experimental design. M.Y.Z. designed the MHC-I/II DKO BMDC-T cell co-culture assay. C.E.M designed the nanopore sequencing approach. A.N., G.B., J.Br., V.P., and L.S. participated the project discussion. B.Z.S. provided KPCY cells. Y.A. and M.O. provided PyMT cells. J. Bu., D.R.J., L.S., M.Y.Z., S.C., V.P., C.E.M., I.R.M., H.Z., and D.L. read the manuscript and provided feedback. D.L. led the project.

DECLARATION OF INTERESTS

The authors declare no competing interests.

STAR★METHODS

Detailed methods are provided in the online version of this paper and include the following:

- KEY RESOURCES TABLE
- EXPERIMENTAL MODEL AND STUDY PARTICIPANT DETAILS
  - Human studies
  - Cell culture
  - Mouse studies
- METHOD DETAILS
  - Generation of NLS-GFP-expressing 4T1 and STING-knockout BlaER1 cell lines
  - EV purification, characterization and labelling
  - EV_{DNA} extraction, characterization and digestion
  - BrdU pulse chase study
  - *In vitro* education with T cell-derived EVs
  - Coculture of BMDCs and naïve T cells
  - Treatment of DC2.4 cells
  - EV_{DNA} and EV_{RNA} transfection with lipofectamine 3000
  - Cell migration assays
  - Gzmb inhibitor screening assay
  - Subcellular distribution of T cell-derived EV_{DNA}
  - Enzyme-linked immunosorbent assay
  - Western blotting
  - RNA extraction and RT-qPCR analysis
  - Flow cytometry
  - Tissue processing and immunofluorescence staining
  - Biodistribution assessment
  - Tumor models and *in vivo* treatments
  - RNAseq and bioinformatic analysis
  - WGS and bioinformatics analysis
  - Sample preparation for mass spectrometry (MS), MS data processing and proteomics data analysis
  - Nanopore sequencing and bioinformatics analysis
- QUANTIFICATION AND STATISTICAL ANALYSIS

SUPPLEMENTAL INFORMATION

Supplemental information can be found online at https://doi.org/10.1016/j.ccell.2026.03.023.

Received: July 24, 2024
Revised: August 2, 2025
Accepted: March 31, 2026
Published: April 30, 2026

REFERENCES

1. Yang, K., Halima, A., and Chan, T.A. (2023). Antigen presentation in cancer—mechanisms and clinical implications for immunotherapy. Nat. Rev. Clin. Oncol. *20*, 604–623.
2. Jhunjhunwala, S., Hammer, C., and Delamarre, L. (2021). Antigen presentation in cancer: insights into tumour immunogenicity and immune evasion. Nat. Rev. Cancer *21*, 298–312.
3. Hodi, F.S., O'day, S.J., McDermott, D.F., Weber, R.W., Sosman, J.A., Haanen, J.B., Gonzalez, R., Robert, C., Schadendorf, D., Hassel, J.C., et al. (2010). Improved survival with ipilimumab in patients with metastatic melanoma. N. Engl. J. Med. Overseas. Ed. *363*, 711–723.
4. Larkin, J., Chiarion-Sileni, V., Gonzalez, R., Grob, J.J., Cowey, C.L., Lao, C.D., Schadendorf, D., Dummer, R., Smylie, M., Rutkowski, P., et al. (2015). Combined nivolumab and ipilimumab or monotherapy in untreated melanoma. N. Engl. J. Med. *373*, 23–34.
5. Yamamoto, K., Venida, A., Yano, J., Biancur, D.E., Kakiuchi, M., Gupta, S., Sohn, A.S.W., Mukhopadhyay, S., Lin, E.Y., Parker, S.J., et al. (2020). Autophagy promotes immune evasion of pancreatic cancer by degrading MHC-I. Nature *581*, 100–105.
6. Fangazio, M., Ladewig, E., Gomez, K., Garcia-Ibanez, L., Kumar, R., Teruya-Feldstein, J., Rossi, D., Filip, I., Pan-Hammarström, Q., Inghirami, G., et al. (2021). Genetic mechanisms of HLA-I loss and immune escape in diffuse large B cell lymphoma. Proc. Natl. Acad. Sci. USA *118*, e2104504118.
7. Beyaz, S., Chung, C., Mou, H., Bauer-Rowe, K.E., Xifaras, M.E., Ergin, I., Dohnalova, L., Biton, M., Shekhar, K., Eskiocak, O., et al. (2021). Dietary suppression of MHC class II expression in intestinal epithelial cells enhances intestinal tumorigenesis. Cell Stem Cell *28*, 1922–1935.e5.
8. Hu, Q., Ye, Y., Chan, L.-C., Li, Y., Liang, K., Lin, A., Egranov, S.D., Zhang, Y., Xia, W., Gong, J., et al. (2019). Oncogenic lncRNA downregulates cancer cell antigen presentation and intrinsic tumor suppression. Nat. Immunol. *20*, 835–851.
9. Mahadevan, N.R., Knelson, E.H., Wolff, J.O., Vajdi, A., Saigí, M., Campisi, M., Hong, D., Thai, T.C., Piel, B., Han, S., et al. (2021). Intrinsic immunogenicity of small cell lung carcinoma revealed by its cellular plasticity. Cancer Discov. *11*, 1952–1969.
10. Burr, M.L., Sparbier, C.E., Chan, K.L., Chan, Y.-C., Kersbergen, A., Lam, E.Y.N., Azidis-Yates, E., Vassiliadis, D., Bell, C.C., Gilan, O., et al. (2019). An evolutionarily conserved function of polycomb silences the MHC class I antigen presentation pathway and enables immune evasion in cancer. Cancer Cell *36*, 385–401.e8.
11. Hangai, S., Ao, T., Kimura, Y., Matsuki, K., Kawamura, T., Negishi, H., Nishio, J., Kodama, T., Taniguchi, T., and Yanai, H. (2016). PGE2 induced in and released by dying cells functions as an inhibitory DAMP. Proc. Natl. Acad. Sci. USA *113*, 3844–3849.
12. Gabrilovich, D.I., Chen, H.L., Girgis, K.R., Cunningham, H.T., Meny, G.M., Nadaf, S., Kavanaugh, D., and Carbone, D.P. (1996). Production of

vascular endothelial growth factor by human tumors inhibits the functional maturation of dendritic cells. Nat. Med. *2*, 1096–1103.

13. Papaspyridonos, M., Matei, I., Huang, Y., do Rosario Andre, M., Brazier-Mitouart, H., Waite, J.C., Chan, A.S., Kalter, J., Ramos, I., Wu, Q., et al. (2015). Id1 suppresses anti-tumour immune responses and promotes tumour progression by impairing myeloid cell maturation. Nat. Commun. *6*, 6840.
14. Herber, D.L., Cao, W., Nefedova, Y., Novitskiy, S.V., Nagaraj, S., Tyurin, V.A., Corzo, A., Cho, H.-I., Celis, E., Lennox, B., et al. (2010). Lipid accumulation and dendritic cell dysfunction in cancer. Nat. Med. *16*, 880–886.
15. Gao, J., Shi, L.Z., Zhao, H., Chen, J., Xiong, L., He, Q., Chen, T., Roszik, J., Bernatchez, C., Woodman, S.E., et al. (2016). Loss of IFN-γ pathway genes in tumor cells as a mechanism of resistance to anti-CTLA-4 therapy. Cell *167*, 397–404.e9.
16. Zaretsky, J.M., Garcia-Diaz, A., Shin, D.S., Escuin-Ordinas, H., Hugo, W., Hu-Lieskovan, S., Torrejon, D.Y., Abril-Rodriguez, G., Sandoval, S., Barthly, L., et al. (2016). Mutations associated with acquired resistance to PD-1 blockade in melanoma. N. Engl. J. Med. *375*, 819–829.
17. Gocher, A.M., Workman, C.J., and Vignali, D.A.A. (2022). Interferon-γ: teammate or opponent in the tumour microenvironment? Nat. Rev. Immunol. *22*, 158–172.
18. Giannopoulos, A., Constantinides, C., Fokaeas, E., Stravodimos, C., Giannopoulou, M., Kyroudi, A., and Gounaris, A. (2003). The immunomodulating effect of interferon-γ intravesical instillations in preventing bladder cancer recurrence. Clin. Cancer Res. *9*, 5550–5558.
19. Windbichler, G.H., Hausmaninger, H., Stummvoll, W., Graf, A.H., Kainz, C., Lahodny, J., Denison, U., Müller-Holzner, E., and Marth, C. (2000). Interferon-gamma in the first-line therapy of ovarian cancer: a randomized phase III trial. Br. J. Cancer *82*, 1138–1144.
20. Alberts, D.S., Marth, C., Alvarez, R.D., Johnson, G., Bidzinski, M., Kardatzke, D.R., Bradford, W.Z., Loutit, J., Kirn, D.H., Clouser, M.C., et al. (2008). Randomized phase 3 trial of interferon gamma-1b plus standard carboplatin/paclitaxel versus carboplatin/paclitaxel alone for first-line treatment of advanced ovarian and primary peritoneal carcinomas: results from a prospectively designed analysis of progression-free survival. Gynecol. Oncol. *109*, 174–181.
21. Hu, M., Kenific, C.M., Boudreau, N., and Lyden, D. (2023). Tumor-derived Nanoseeds Condition the Soil for Metastatic Organotropism (Elsevier), pp. 70–82.
22. Thakur, B.K., Zhang, H., Becker, A., Matei, I., Huang, Y., Costa-Silva, B., Zheng, Y., Hoshino, A., Brazier, H., Xiang, J., et al. (2014). Double-stranded DNA in exosomes: a novel biomarker in cancer detection. Cell Res. *24*, 766–769.
23. Sansone, P., Savini, C., Kurelac, I., Chang, Q., Amato, L.B., Strillacci, A., Stepanova, A., Iommarini, L., Mastroleo, C., Daly, L., et al. (2017). Packaging and transfer of mitochondrial DNA via exosomes regulate escape from dormancy in hormonal therapy-resistant breast cancer. Proc. Natl. Acad. Sci. USA *114*, E9066–E9075.
24. Wortzel, I., Seo, Y., Akano, I., Shaashua, L., Tobias, G.C., Hebert, J., Kim, K.-A., Kim, D., Dror, S., Liu, Y., et al. (2024). Unique structural configuration of EV-DNA primes Kupffer cell-mediated antitumor immunity to prevent metastatic progression. Nat. Cancer *5*, 1815–1833.
25. Garcia, K.C., Teyton, L., and Wilson, I.A. (1999). Structural basis of T cell recognition. Annu. Rev. Immunol. *17*, 369–397.
26. Mantovani, A., Dinarello, C.A., Molgora, M., and Garlanda, C. (2019). Interleukin-1 and related cytokines in the regulation of inflammation and immunity. Immunity *50*, 778–795.
27. Vanderbeck, A., and Maillard, I. (2021). Notch signaling at the crossroads of innate and adaptive immunity. J. Leukoc. Biol. *109*, 535–548.
28. Pagliari, D., Cianci, R., Frosali, S., Landolfi, R., Cammarota, G., Newton, E.E., and Pandolfi, F. (2013). The role of IL-15 in gastrointestinal diseases: a bridge between innate and adaptive immune response. Cytokine Growth Factor Rev. *24*, 455–466.
29. Iwasaki, A., and Medzhitov, R. (2015). Control of adaptive immunity by the innate immune system. Nat. Immunol. *16*, 343–353.
30. Maas, S.L.N., Breakefield, X.O., and Weaver, A.M. (2017). Extracellular vesicles: unique intercellular delivery vehicles. Trends Cell Biol. *27*, 172–188.
31. Lanna, A., Vaz, B., D'Ambra, C., Valvo, S., Vuotto, C., Chiurchiù, V., Devine, O., Sanchez, M., Borsellino, G., Akbar, A.N., et al. (2022). An intercellular transfer of telomeres rescues T cells from senescence and promotes long-term immunological memory. Nat. Cell Biol. *24*, 1461–1474.
32. Wang, G., Li, J., Bojmar, L., Chen, H., Li, Z., Tobias, G.C., Hu, M., Homan, E.A., Lucotti, S., Zhao, F., et al. (2023). Tumour extracellular vesicles and particles induce liver metabolic dysfunction. Nature *618*, 374–382.
33. Bojmar, L., Kim, H.S., Tobias, G.C., Pelissier Vatter, F.A., Lucotti, S., Gyan, K.E., Kenific, C.M., Wan, Z., Kim, K.-A., Kim, D., et al. (2021). Extracellular vesicle and particle isolation from human and murine cell lines, tissues, and bodily fluids. STAR Protoc. *2*, 100225.
34. Hoshino, A., Kim, H.S., Bojmar, L., Gyan, K.E., Cioffi, M., Hernandez, J., Zambirinis, C.P., Rodrigues, G., Molina, H., Heissel, S., et al. (2020). Extracellular vesicle and particle biomarkers define multiple human cancers. Cell *182*, 1044–1061.e18.
35. Gaidt, M.M., Rapino, F., Graf, T., and Hornung, V. (2018). Modeling primary human monocytes with the trans–differentiation cell line BLaER1. Innate Immune Activation. Methods Mol. Biol. *1714*, 57–66.
36. Wang, Y., Tiruthani, K., Li, S., Hu, M., Zhong, G., Tang, Y., Roy, S., Zhang, L., Tan, J., Liao, C., and Liu, R. (2021). mRNA delivery of a bispecific single-domain antibody to polarize tumor-associated macrophages and synergize immunotherapy against liver malignancies. Adv. Mater. *33*, 2007603.
37. Zhang, H., Freitas, D., Kim, H.S., Fabijanic, K., Li, Z., Chen, H., Mark, M.T., Molina, H., Martin, A.B., Bojmar, L., et al. (2018). Identification of distinct nanoparticles and subsets of extracellular vesicles by asymmetric flow field-flow fractionation. Nat. Cell Biol. *20*, 332–343.
38. Kalbasi, A., and Ribas, A. (2020). Tumour-intrinsic resistance to immune checkpoint blockade. Nat. Rev. Immunol. *20*, 25–39.
39. Wiklander, O.P.B., Nordin, J.Z., O'Loughlin, A., Gustafsson, Y., Corso, G., Mäger, I., Vader, P., Lee, Y., Sork, H., Seow, Y., et al. (2015). Extracellular vesicle *in vivo* biodistribution is determined by cell source, route of administration and targeting. J. Extracell. Vesicles *4*, 26316.
40. Qiao, L., Hu, S., Huang, K., Su, T., Li, Z., Vandergriff, A., Cores, J., Dinh, P.-U., Allen, T., Shen, D., et al. (2020). Tumor cell-derived exosomes home to their cells of origin and can be used as Trojan horses to deliver cancer drugs. Theranostics *10*, 3474–3487.
41. Roland, C.L., Harken, A.H., Sarr, M.G., and Barnett, C.C., Jr. (2007). ICAM-1 expression determines malignant potential of cancer. Surgery *141*, 705–707.
42. Hayes, S.H., and Seigel, G.M. (2009). Immunoreactivity of ICAM-1 in human tumors, metastases and normal tissues. Int. J. Clin. Exp. Pathol. *2*, 553–560.
43. Leinwand, J., and Miller, G. (2020). Regulation and modulation of antitumor immunity in pancreatic cancer. Nat. Immunol. *21*, 1152–1159.
44. Li, J., Byrne, K.T., Yan, F., Yamazoe, T., Chen, Z., Baslan, T., Richman, L.P., Lin, J.H., Sun, Y.H., Rech, A.J., et al. (2018). Tumor cell-intrinsic factors underlie heterogeneity of immune cell infiltration and response to immunotherapy. Immunity *49*, 178–193.e7.
45. Genoud, V., Marinari, E., Nikolaev, S.I., Castle, J.C., Bukur, V., Dietrich, P.-Y., Okada, H., and Walker, P.R. (2018). Responsiveness to anti-PD-1 and anti-CTLA-4 immune checkpoint blockade in SB28 and GL261 mouse glioma models. OncoImmunology *7*, e1501137.
46. Schumacher, T.N., and Thommen, D.S. (2022). Tertiary lymphoid structures in cancer. Science *375*, eabf9419.
47. Arens, R., and Scheeren, F.A. (2020). Genetic screening for novel regulators of immune checkpoint molecules. Trends Immunol. *41*, 692–705.
48. Jorgovanovic, D., Song, M., Wang, L., and Zhang, Y. (2020). Roles of IFN-γ in tumor progression and regression: a review. Biomark. Res. *8*, 49.

49. Kobayashi, K.S., and Van Den Elsen, P.J. (2012). NLRC5: a key regulator of MHC class I-dependent immune responses. Nat. Rev. Immunol. *12*, 813–820.

50. Vijayan, S., Sidiq, T., Yousuf, S., van den Elsen, P.J., and Kobayashi, K.S. (2019). Class I transactivator, NLRC5: a central player in the MHC class I pathway and cancer immune surveillance. Immunogenetics *71*, 273–282.

51. Emming, S., and Schroder, K. (2019). Tiered DNA sensors for escalating responses. Science *365*, 1375–1376.

52. Li, T., Cheng, H., Yuan, H., Xu, Q., Shu, C., Zhang, Y., Xu, P., Tan, J., Rui, Y., Li, P., and Tan, X. (2016). Antitumor activity of cGAMP via stimulation of cGAS-cGAMP-STING-IRF3 mediated innate immune response. Sci. Rep. *6*, 19049.

53. Temizoz, B., Kuroda, E., Ohata, K., Jounai, N., Ozasa, K., Kobiyama, K., Aoshi, T., and Ishii, K.J. (2015). TLR9 and STING agonists synergistically induce innate and adaptive type-II IFN. Eur. J. Immunol. *45*, 1159–1169.

54. Rathinam, V.A.K., Jiang, Z., Waggoner, S.N., Sharma, S., Cole, L.E., Waggoner, L., Vanaja, S.K., Monks, B.G., Ganesan, S., Latz, E., et al. (2010). The AIM2 inflammasome is essential for host defense against cytosolic bacteria and DNA viruses. Nat. Immunol. *11*, 395–402.

55. Tanaka, Y., and Chen, Z.J. (2012). STING specifies IRF3 phosphorylation by TBK1 in the cytosolic DNA signaling pathway. Sci. Signal. *5*, ra20.

56. Santegoets, S.J.A.M., Turksma, A.W., Suhoski, M.M., Stam, A.G.M., Albelda, S.M., Hooijberg, E., Scheper, R.J., van den Eertwegh, A.J.M., Gerritsen, W.R., Powell, D.J., Jr., et al. (2013). IL-21 promotes the expansion of CD27+ CD28+ tumor infiltrating lymphocytes with high cytotoxic potential and low collateral expansion of regulatory T cells. J. Transl. Med. *11*, 37.

57. Nurieva, R., Yang, X.O., Martinez, G., Zhang, Y., Panopoulos, A.D., Ma, L., Schluns, K., Tian, Q., Watowich, S.S., Jetten, A.M., and Dong, C. (2007). Essential autocrine regulation by IL-21 in the generation of inflammatory T cells. Nature *448*, 480–483.

58. Zhang, D., Beresford, P.J., Greenberg, A.H., and Lieberman, J. (2001). Granzymes A and B directly cleave lamins and disrupt the nuclear lamina during granule-mediated cytolysis. Proc. Natl. Acad. Sci. USA *98*, 5746–5751.

59. Boivin, W.A., Cooper, D.M., Hiebert, P.R., and Granville, D.J. (2009). Intracellular versus extracellular granzyme B in immunity and disease. Lab. Invest. *89*, 1195–1220.

60. Denais, C.M., Gilbert, R.M., Isermann, P., McGregor, A.L., Te Lindert, M., Weigelin, B., Davidson, P.M., Friedl, P., Wolf, K., and Lammerding, J. (2016). Nuclear envelope rupture and repair during cancer cell migration. Science *352*, 353–358.

61. Ivančić, D., Mir-Pedrol, J., Jaraba-Wallace, J., Rafel, N., Sanchez-Mejias, A., and Güell, M. (2022). INSERT-seq enables high-resolution mapping of genomically integrated DNA using Nanopore sequencing. Genome Biol. *23*, 227.

62. Hoshino, A., Costa-Silva, B., Shen, T.-L., Rodrigues, G., Hashimoto, A., Tesic Mark, M., Molina, H., Kohsaka, S., Di Giannatale, A., Ceder, S., et al. (2015). Tumour exosome integrins determine organotropic metastasis. Nature *527*, 329–335.

63. González-Amaro, R., and Sanchez-Madrid, F. (1999). Cell adhesion molecules: selectins and integrins. Crit. Rev. Immunol. *19*, 389.

64. Torralba, D., Baixauli, F., Villarroya-Beltri, C., Fernández-Delgado, I., Latorre-Pellicer, A., Acín-Pérez, R., Martín-Cófreces, N.B., Jaso-Tamame, Á.L., Iborra, S., Jorge, I., et al. (2018). Priming of dendritic cells by DNA-containing extracellular vesicles from activated T cells through antigen-driven contacts. Nat. Commun. *9*, 2658.

65. Diamond, J.M., Vanpouille-Box, C., Spada, S., Rudqvist, N.-P., Chapman, J.R., Ueberheide, B.M., Pilones, K.A., Sarfraz, Y., Formenti, S.C., and Demaria, S. (2018). Exosomes shuttle TREX1-sensitive IFN-stimulatory dsDNA from irradiated cancer cells to DCs. Cancer Immunol. Res. *6*, 910–920.

66. Michalski, S., de Oliveira Mann, C.C., Stafford, C.A., Witte, G., Bartho, J., Lammens, K., Hornung, V., and Hopfner, K.-P. (2020). Structural basis for sequestration and autoinhibition of cGAS by chromatin. Nature *587*, 678–682.

67. Zierhut, C., Yamaguchi, N., Paredes, M., Luo, J.-D., Carroll, T., and Funabiki, H. (2019). The cytoplasmic DNA sensor cGAS promotes mitotic cell death. Cell *178*, 302–315.e23.

68. Li, T., Huang, T., Du, M., Chen, X., Du, F., Ren, J., and Chen, Z.J. (2021). Phosphorylation and chromatin tethering prevent cGAS activation during mitosis. Science *371*, eabc5386.

69. Buck, J., Grossen, P., Cullis, P.R., Huwyler, J., and Witzigmann, D. (2019). Lipid-based DNA therapeutics: hallmarks of non-viral gene delivery. ACS Nano *13*, 3754–3782.

70. Hajj, K.A., and Whitehead, K.A. (2017). Tools for translation: non-viral materials for therapeutic mRNA delivery. Nat. Rev. Mater. *2*, 17056.

71. Liu, M.A. (2019). A comparison of plasmid DNA and mRNA as vaccine technologies. Vaccines *7*, 37.

72. Hu, Z., Chen, H., Long, Y., Li, P., and Gu, Y. (2021). The main sources of circulating cell-free DNA: apoptosis, necrosis and active secretion. Crit. Rev. Oncol. Hematol. *157*, 103166.

73. Rogers, J.C., Boldt, D., Kornfeld, S., Skinner, A., and Valeri, C.R. (1972). Excretion of deoxyribonucleic acid by lymphocytes stimulated with phytohemagglutinin or antigen. Proc. Natl. Acad. Sci. USA *69*, 1685–1689.

74. Perez-Riverol, Y., Bandla, C., Kundu, D.J., Kamatchinathan, S., Bai, J., Hewapathirana, S., John, N.S., Prakash, A., Walzer, M., Wang, S., and Vizcaíno, J.A. (2025). The PRIDE database at 20 years: 2025 update. Nucleic Acids Res. *53*, D543–D553.

75. Ying, W., Cheruku, P.S., Bazer, F.W., Safe, S.H., and Zhou, B. (2013). Investigation of macrophage polarization using bone marrow derived macrophages. JoVE J. *76*, 50323.e50323.

76. Endo, S., Sakamoto, Y., Kobayashi, E., Nakamura, A., and Takai, T. (2008). Regulation of cytotoxic T lymphocyte triggering by PIR-B on dendritic cells. Proc. Natl. Acad. Sci. USA *105*, 14515–14520.

77. Ueda, J., Saito, H., Watanabe, H., and Evers, B.M. (2005). Novel and quantitative DNA dot-blotting method for assessment of *in vivo* proliferation. Am. J. Physiol. Gastrointest. Liver Physiol. *288*, G842–G847.

78. Livak, K.J., and Schmittgen, T.D. (2001). Analysis of relative gene expression data using real-time quantitative PCR and the $2^{-\Delta\Delta CT}$ method. methods *25*, 402–408.

79. Anand, L., and Rodriguez Lopez, C.M. (2022). ChromoMap: an R package for interactive visualization of multi-omics data and annotation of chromosomes. BMC Bioinf. *23*, 33.

80. McKenna, A., Hanna, M., Banks, E., Sivachenko, A., Cibulskis, K., Kernytsky, A., Garimella, K., Altshuler, D., Gabriel, S., Daly, M., and DePristo, M.A. (2010). The Genome Analysis Toolkit: a MapReduce framework for analyzing next-generation DNA sequencing data. Genome Res. *20*, 1297–1303.

81. DePristo, M.A., Banks, E., Poplin, R., Garimella, K.V., Maguire, J.R., Hartl, C., Philippakis, A.A., Del Angel, G., Rivas, M.A., Hanna, M., et al. (2011). A framework for variation discovery and genotyping using next-generation DNA sequencing data. Nat. Genet. *43*, 491–498.

82. Graw, S., Tang, J., Zafar, M.K., Byrd, A.K., Bolden, C., Peterson, E.C., and Byrum, S.D. (2020). proteiNorm–A user-friendly tool for normalization and analysis of TMT and label-free protein quantification. ACS Omega *5*, 25625–25633.

83. Aguilan, J.T., Kulej, K., and Sidoli, S. (2020). Guide for protein fold change and p-value calculation for non-experts in proteomics. Mol. Omics *16*, 573–582.

84. Babicki, S., Arndt, D., Marcu, A., Liang, Y., Grant, J.R., Maciejewski, A., and Wishart, D.S. (2016). Heatmapper: web-enabled heat mapping for all. Nucleic Acids Res. *44*, W147–W153.

STAR★METHODS

KEY RESOURCES TABLE

REAGENT or RESOURCE	SOURCE	IDENTIFIER
Antibodies		
TruStain FcX™ PLUS (anti-mouse CD16/32) Antibody (clone S17011E)	Biolegend	Cat#156603; RRID: AB_2783137
Brilliant Violet 510™ anti-mouse CD45 Antibody (clone 30-F11)	Biolegend	Cat#103138; RRID: AB_2563061
Alexa Fluor® 647 anti-mouse CD3 Antibody (clone 17A2)	Biolegend	Cat#100209; RRID: AB_389323
Brilliant Violet 650™ anti-mouse/human CD45R/B220 Antibody (clone RA3-6B2)	Biolegend	Cat#103241; RRID: AB_11204069
PerCP/Cyanine5.5 anti-mouse CD4 Antibody (clone GK1.5)	Biolegend	Cat#100434; RRID: AB_893324
PE/Cyanine7 anti-mouse CD8a Antibody (clone 53–6.7)	Biolegend	Cat#100722; RRID: AB_312761
PerCP/Cyanine5.5 anti-mouse/human CD11b Antibody (clone M1/70)	Biolegend	Cat#101228; RRID: AB_893232
PE/Cyanine7 anti-mouse CD11c Antibody (clone N418)	Biolegend	Cat#117318; RRID: AB_493568
Brilliant Violet 421™ anti-mouse Ly-6G Antibody (clone 1A8)	Biolegend	Cat#127628; RRID: AB_2562567
Alexa Fluor® 647 anti-mouse Ly-6C Antibody (clone HK1.4)	Biolegend	Cat#128010; RRID: AB_1236550
Brilliant Violet 650™ anti-mouse F4/80 Antibody (clone BM8)	Biolegend	Cat#123149; RRID: AB_2564589
PE anti-mouse CD206 (MMR) Antibody (clone C068C2)	Biolegend	Cat#141706; RRID: AB_10895754
PE anti-mouse IFN-γ Antibody (clone XMG1.2)	Biolegend	Cat#505807; RRID: AB_315401
PE anti-mouse NK-1.1 Antibody (clone PK136)	Biolegend	Cat#108708; RRID: AB_313395
Alexa Fluor® 700 anti-mouse CD86 Antibody (clone GL-1)	Biolegend	Cat#105024; RRID: AB_493721
Brilliant Violet 421™ anti-mouse I-A/I-E Antibody (clone M5/114.15.2)	Biolegend	Cat#107632; RRID: AB_2650896
FITC anti-mouse I-A/I-E Antibody (clone M5/114.15.2)	Biolegend	Cat#107606; RRID: AB_313321
APC anti-mouse H-2Kb Antibody (clone AF6-88.5)	Biolegend	Cat#116518; RRID: AB_10564404
PE anti-mouse H-2Kd Antibody (clone SF1-1.1)	Biolegend	Cat#116608; RRID: AB_313743
PE anti-mouse CD31 Antibody (clone 390)	Biolegend	Cat#102408; RRID: AB_312903
FITC anti-mouse CD279 (PD-1) Antibody (clone 29F.1A12)	Biolegend	Cat#135214; RRID: AB_10680238
APC anti-human HLA-DR, DP, DQ Antibody (clone Tü39)	Biolegend	Cat#361713; RRID: AB_2750315
PE anti-human HLA-A,B,C Antibody (clone W6/32)	Biolegend	Cat#311406; RRID: 314875
Purified anti-mouse/human CD45R/B220 Antibody (clone RA3-6B2)	Biolegend	Cat#103201; RRID: AB_312986
Alexa Fluor® 647 anti-human CD3 Antibody (clone UCHT1)	Biolegend	Cat#300416; RRID: AB_389332

(*Continued on next page*)

Continued

REAGENT or RESOURCE	SOURCE	IDENTIFIER
Mouse Fibroblast Activation Protein alpha/ FAP Alexa Fluor® 647-conjugated Antibody	R&D Systems	Cat#FAB9727R; RRID: AB_3654151
PE-Labeled Mouse H-2Kb&B2M&OVA (SIINFEKL) Tetramer Protein	ACROBiosystems	Cat#H2A-MP2H7
CD21 Recombinant Rabbit Monoclonal Antibody (SC0681)	Invitrogen	Cat#MA5-32227
Goat anti-Mouse IgG (H + L) Cross-Adsorbed Secondary Antibody, Alexa Fluor™ 488	Invitrogen	Cat#A-11001
Goat anti-Rabbit IgG (H + L) Cross-Adsorbed Secondary Antibody, Alexa Fluor™ 555	Invitrogen	Cat#A-21428
Alexa Fluor™ 594 Phalloidin	Invitrogen	Cat#A12381
GAPDH Loading Control Monoclonal Antibody (GA1R)	Invitrogen	Cat#MA5-15738
TMEM173/STING Polyclonal antibody	Proteintech	Cat#19851-1-AP
Phospho-STING (Ser365) (D8F4W) Rabbit mAb	Cell Signaling Technology	Cat#72971; RRID: AB_2799831
TBK1/NAK (D1B4) Rabbit mAb	Cell Signaling Technology	Cat#3504; RRID: AB_2255663
Phospho-TBK1/NAK (Ser172) (D52C2) XP® Rabbit mAb	Cell Signaling Technology	Cat#5483; RRID: AB_10693472
Anti-rabbit IgG, HRP-linked Antibody	Cell Signaling Technology	Cat#7074; RRID: AB_2099233
Anti-mouse IgG, HRP-linked Antibody	Cell Signaling Technology	Cat#7076; RRID: AB_330924
Biological samples		
Human glioma samples, See Table S2	NCI Cooperative Human Tissue Network (CHTN)	N/A
Human pancreatic cancer samples, See Table S2	Memorial Sloan Kettering Cancer Center	N/A
Critical commercial assays		
Agencourt AMPure XP	Beckman Coulter	Cat#A63881
Pan T cell Isolation Kit II, mouse	Miltenyi Biotec	Cat#130-095-130
$CD4^+$ T cell Isolation Kit, mouse	Miltenyi Biotec	Cat#130-104-454
$CD8a^+$ T cell Isolation Kit, mouse	Miltenyi Biotec	Cat#130-104-075
Pan T cell Isolation Kit, human	Miltenyi Biotec	Cat#130-096-535
B Cell Isolation Kit, mouse	Miltenyi Biotec	Cat#130-090-862
EasySep™ Mouse Pan-Naïve T cell Isolation Kit	STEMCELL Technologies	Cat#19848
EasySep™ Mouse Neutrophil Enrichment Kit	STEMCELL Technologies	Cat#19762
Dynabeads™ Human T-Activator CD3/ CD28 for T cell Expansion and Activation	ThermoFisher Scientific	Cat#11132
Dynabeads™ Mouse T-Activator CD3/CD28 for T cell Expansion and Activation	ThermoFisher Scientific	Cat#11453
Human IL-2 Recombinant Protein, PeproTech®	ThermoFisher Scientific	Cat#200-02
Mouse IL-2 Recombinant Protein, PeproTech®	ThermoFisher Scientific	Cat#212-12
Granzyme B Inhibitor Screening Kit	Sigma-Aldrich	Cat#MAK209
mouse IFN-gamma quantikine ELISA kit	R&D Systems	Cat#MIF00
RNeasy Plus Mini kit	Qiagen	Cat#74134
iScript™ cDNA Synthesis Kit	Bio-Rad	Cat#1708890
SYBR Green Supermix	Bio-Rad	Cat#1725271

(*Continued on next page*)

Continued

REAGENT or RESOURCE	SOURCE	IDENTIFIER
Lipofectamine™ LTX Reagent with PLUS™ Reagent	Invitrogen	Cat#15338030
Lipofectamine™ 3000 Transfection Reagent	Invitrogen	Cat#L3000001
Recombinant DNA		
pCDH-NLS-copGFP-EF1-BlastiS	Addgene	132772
psPAX2	Addgene	12260
pMD2.G	Addgene	12259
pRRE	Addgene	12251
pRSV-REV	Addgene	12253
Experimental models: Cell lines		
Mouse: KPCY cell clones	Dr. Ben Z. Stanger[44]	N/A
Mouse: PyMT cells	Dr. Yael Aylon	N/A
Mouse: TK1	ATCC	CRL-2396
Mouse: Raw264.7	ATCC	TIB-71
Mouse: NIH/3T3	ATCC	CRL-1658
Mouse: CT26 wild-type	ATCC	CRL-2638
Mouse: 4T1	ATCC	CRL-2539
Mouse: B16F10	ATCC	CRL-6475
Mouse: DC2.4	Sigma-Aldrich	SCC142
Mouse: SB28-Ohlfest	Leibniz Institute DSMZ	ACC880
Human: BCL2 Jurkat	ATCC	CRL-2899
Human: NALM6	ATCC	CRL-3273
Human: HT29	ATCC	HTB-38
Human: MAD-MB-231	ATCC	HTB-26
Human: DAOY	ATCC	HTB-186
Human: BlaER1	Sigma-Aldrich	SCC165
Human: LX-2	Sigma-Aldrich	SCC064
Experimental models: Organisms/strains		
Mouse: wild-type C57BL/6	Jackson Laboratory	000664
Mouse: wild-type BALB/c	Jackson Laboratory	000651
Mouse: wild-type FVB/NJ	Jackson Laboratory	001800
Mouse: NSG-MHC-I/II DKO	Jackson Laboratory	025216
Mouse: OT-II	Jackson Laboratory	004194
Deposited data		
RNAseq data	This paper	Gene Expression Omnibus: GSE290812, GSE290972, GSE291466, GSE325678.
WGS data	This paper	NIH BioProject: PRJNA1135491, PRJNA1231632
Nanopore sequencing data	This paper	European Nucleotide Archive: PRJEB83979
Proteomics data	This paper	PXD075986, PXD075814
Software and algorithms		
Image Studio™	LI-COR	V5.2
ImageJ	National Institutes of Health	1.48v
FlowJo	FlowJo	V10
R	The R Foundation	V4.2.2
Python	Python.org	V3.12.0
GSEA	https://www.gsea-msigdb.org/gsea/index.jsp	v4.2.2
Graphpad Prism	Graphpad	V8

EXPERIMENTAL MODEL AND STUDY PARTICIPANT DETAILS

Human studies

Fresh glioma specimens were obtained from NCI Cooperative Human Tissue Network (CHTN) using the standard biorepository protocol from patients undergoing surgery for glioblastoma, astrocytoma, or undefined glioma under WCM IRB 0604008488. Fresh pancreatic tumors were obtained intraoperatively at Memorial Sloan Kettering Cancer Center (MSKCC) (IRB15-015) from patients undergoing pancreatectomy for localized resectable pancreatic cancer. All the patients gave consent for research use of the biospecimens. None of the patients had any evidence of distant metastasis at the time of surgery. De-identified patient information was described in Table S2. Glioma samples were shipped in RPMI serum-free medium on ice and processed for tissue explant culture and cryosections after overnight delivery. Pancreatic tumors were processed for tissue explant culture and paraffin embedding immediately after the surgery. All patient specimen-associated experiments were performed according to the protocol approved by the Institutional Review Boards of Weill Cornell Medicine (IRB 0604008488). The study is compliant with all relevant ethical regulations regarding research involving human participants.

Cell culture

TK1, Raw264.7, 3T3 (NIH/3T3), CT26, 4T1, B16F10, Jurkat (BCL2 Jurkat), NALM6, HT29, MAD-MB-231, DAOY and 293T cells were purchased from American Type Culture Collection. DC2.4, BlaER1 and LX-2 cells were purchased from Sigma-Aldrich. The SB28 (SB28-Ohlfest) cell line was purchased from the Leibniz Institute DSMZ. Human primary macrophage cells were purchased from Celprogen (36070-01). KPCY cell clones (6419c5, 6694c2, 6421c1, 6421c2, 2838c3, 6556c4) were obtained from Ben Z. Stanger.[44] TK1, 4T1, Jurkat, NALM6, DC2.4 and BlaER1 cells were cultured in RPMI (Corning, 10-040-CV) supplemented with 10% fetal bovine serum (FBS) (Gibco, 10438-026) and 1× penicillin/streptomycin (P/S) (100 U ml^{-1} of penicillin and 100 μg ml^{-1} of streptomycin, Thermo Fisher Scientific, 15070-063). Raw264.7, 3T3, LX-2, CT26, B16F10, HT29, MAD-MB-231, DAOY, 293T, SB28 and KPCY cells were cultured in DMEM (Corning, 10-013-CV) supplemented with 10% FBS and 1× P/S. Human primary macrophages were cultured on the dish pre-coated with human macrophage primary cell culture extracellular matrix (Celprogen, E36070-01) in human macrophage primary cell culture growth medium (Celprogen, M36070-01) supplemented with 10% FBS. BlaER1 cells were trans-differentiated into monocytes by adding human recombinant IL-3 (10ng mL^{-1}, PeproTech, 200-03), human recombinant macrophage colony-stimulating factor (M-CSF, 10ng mL^{-1}, PeproTech, 300-25) and 100nM β-Estradio (Sigma-Aldrich, E4389) into RPMI complete medium for 6-7 days.

PyMT cells were generated from freshly minced MMTV-PyMT mammary tumors after digestion with 10 mg collagenase A (Roche 10103586001) and 1.5 mg hyaluronidase (H4272-30MG; Sigma-Aldrich). After dissociation, the cells were filtered through 70-μm strainers; washed with DMEM, Hanks' Balanced Salt Solution [+Ca^{2+} +Mg^{2+}] supplemented with 2% FBS and 2% HEPES, and Hanks' solution with 8.29 g Tris-NH4Cl (pH 7.2); and finally resuspended in DMEM. Epithelial cancer cell pellets were obtained by twice pulse centrifugation at 800 g for 5 seconds. The following day, adherent cells were washed aggressively to detach fibroblasts. Initially, the cancer cells were cultured in DMEM supplemented with 15% FBS, 2 mM glutamine, 1× nonessential amino acids, and 1× P/S. After the cultures stabilized, they were acclimated to and propagated in DMEM supplemented with 10% FBS and 1× P/S.

Mouse bone marrow derived macrophages (BMDMs) were collected from adult C57BL/6 mice (female, 8-12 weeks old) and prepared following an established protocol.[75] Femurs and tibiae were collected and bone marrow was flushed out with 5 mL ice-cold PBS containing 2% heat inactivated FBS using a sterile syringe and a 21G needle. The bone marrow suspension was filtered through a 40 μm cell strainer into a 50 ml centrifuge tube to remove solid fragments. The filtrate was centrifuged at 450g for 10 min at 4°C, and pellets were dissociated in 10 mL ACK lysing buffer (Gibco, A10492-01) for 5 min. After centrifugation, cells were resuspended in RPMI culture medium supplemented with 10% FBS, 1× P/S, and 20ng mL^{-1} mouse recombinant M-CSF (R&D Systems, 416-ML) and distributed into 100 mm Petri-dishes at a density of 3 × 10^6 cells per dish. The bone marrow derived cells were cultured for 7 days to differentiate into BMDMs.

Mouse bone marrow derived dendritic cells (BMDCs) were collected from tibia and femur of adult C57BL/6 or NSG-mice (female, 8-12 weeks old). After red blood cell lysis with ACK lysing buffer, bone marrow cells were cultured in RPMI medium supplemented with 10% FBS, 1 × P/S, sodium pyruvate (1mM, Gibco, 11360070), HEPES (10mM, Gibco, 15630080), 2-mercaptoethanol (0.055mM, Gibco, 21985023), and mouse recombinant GM-CSF (20ng mL^{-1}, PeproTech, 315-03) in a 24-well plate at a density of 1× 10^6 cells per well for 5 days. Non-adherent cells were collected on Day 6 for subsequent studies.

Mouse neutrophils were isolated from bone marrow derived cells of adult C57BL/6 mice (female, 8-12 weeks old) by EasySep™ neutrophil enrichment kit (Stemcell, 19762) according to the manufacturer's instructions and cultured in RPMI supplemented with 10% FBS and 1× P/S.

Mouse pan T cells were isolated from indicated immune organs (thymus, lymph nodes (a pool of brachial, axillary, inguinal, and cervical lymph nodes), spleens, or mixture of lymph nodes and spleens) of adult mice (female, 8-12 weeks old) by negative magnetic sorting using microbeads according to the manufacturer's instructions (Miltenyi Biotec, 130-095-130). Mouse $CD4^+$ or $CD8^+$ T cells were isolated from a mixture of lymph nodes and spleens from adult C57BL/6 mice (female, 8-12 weeks old) by negative magnetic sorting using microbeads according to the manufacturer's instructions (Miltenyi Biotec, 130-104-454 for $CD4^+$ T cells or 130-104-075 for $CD8^+$ T cells). Mouse pan naïve T cells were isolated from a mixture of lymph nodes and spleens from adult C57BL/6 or BALB/c mice (female, 8-12 weeks old) by negative magnetic sorting using microbeads according to the manufacturer's instructions (Stemcell, 19848). Human peripheral blood samples from de-identified healthy donors were collected by and purchased from the New York

Blood Center. Peripheral blood mononuclear cells (PBMCs) were isolated from the blood samples using Ficoll-Paque™ (Cytiva, 17144003) gradient centrifugation. Human pan T cells were isolated from PBMCs by negative magnetic sorting using microbeads according to the manufacturer's instructions (Miltenyi Biotec, 130-096-535). To obtain non-activated T cell-derived EVs, mouse or human primary T cells were cultured in RPMI supplemented with 10% FBS and 1× P/S without additional supplements for 72h. For AT_{EV} collection, Dynabeads™ Human T-Activator CD3/CD28 beads or Dynabeads™ Mouse T-Activator CD3/CD28 beads (ThermoFisher Scientific) and recombinant IL-2 (50U mL^{-1}, PeproTech, 200-02 for human T cells and 212-12 for mouse T cells) were added to the medium for 72h to generate activated human or mouse T cells. Activated T cell cultures were refreshed with IL-2-supplemented medium (50U mL^{-1}) every 72h. To test antigen-specific T cell activation, pan-T cells isolated from OT-II mice via magnetic bead negative selection (Miltenyi, as described above) were co-cultured in IL-2-supplemented (50U mL^{-1}) RPMI complete medium with irradiated BMDCs[76] that were pre-loaded with chicken ovalbumin (OVA peptide 323-329) ($BMDC\text{-}OVA^{+}$) . Similar to bead-activation, the activated T cell culture was refreshed with IL-2 supplemented medium every 72h. The non-activated control was set by co-culturing OT-II T cells in RMPI complete medium with irradiated BMDCs left unloaded for 72h.

Mouse B cells were isolated from spleens of adult C57BL/6 mice (female, 8-12 weeks old) by negative magnetic sorting using microbeads according to the manufacturer's instructions (Miltenyi Biotec, 130-090-862) and cultured in RPMI supplemented with 10% FBS and 1× P/S. Subsequently, mouse recombinant MEGACD40L® Protein (200ng mL^{-1}, Enzo, ALX-522-120-C010) and IL-4 (50ng mL^{-1}, Biolegend, 574302) were added to the medium for 5 days to generate activated mouse B cells. Human B cells were isolated from PBMCs by immunomagnetic negative selection according to the manufacturer's instructions (Stemcell, 19054) and cultured in RPMI supplemented with 10% FBS and 1× P/S. Subsequently, human recombinant MEGACD40L® Protein (100ng mL^{-1}, Enzo, ALX-522-110-C010) and IL-4 (20ng mL^{-1}, PeproTech, 200-04) were added to the medium for 5 days to generate activated human B cells.

When collecting conditioned medium for EV isolation, FBS was first depleted of EVs by ultracentrifugation at 100,000g for 4 h. Neutrophils were cultured in EV-depleted medium for 24 hours and supernatant was collected for EV isolation. Activated B cells were cultured in EV-depleted medium supplemented with MEGACD40L® and IL-4 for 5 days and supernatant was collected for EV isolation. Activated T cells were cultured in EV-depleted medium supplemented with anti-CD3/CD28 Dynabeads™ or $BMDC\text{-}OVA^{+}$ and IL-2 for 3 days. Subsequently, the cells were replenished with fresh EV-depleted medium containing IL-2 every 3 days. The conditioned medium collected on day 6 and day 9 post T cell activation was pooled for EV isolation. All the other cell types were cultured in EV-depleted medium for 3 days and supernatant was collected before cells reached confluency for EV isolation. Cells were maintained in a humidified 37°C incubator with 5% CO_2, and cell lines routinely tested and confirmed to be negative for mycoplasma.

Mouse studies

Treatment of mice was performed in accordance with institutional, IACUC and AAALAS guidelines. All the mouse studies were performed according to Weill Cornell Medicine animal protocols 0709-666A. All animal experiments were conducted in compliance with relevant ethical regulations regarding animal research. Animals were monitored for stress, illness or abnormal tissue growth, and euthanized if health deteriorated. Mice that died before the experimental endpoint were excluded from the analysis. Female C57BL/6, BALB/c, FVB/NJ, NSG-MHC-I/II DKO (strain #: 025216) mice aged 6-8 weeks were obtained from The Jackson Laboratory and housed in the animal facility under conventional conditions with a light (12 h dark/light circle)-, humidity (30%-70%)- and temperature (21-23°C)-controlled environment.

METHOD DETAILS

Generation of NLS-GFP-expressing 4T1 and STING-knockout BlaER1 cell lines

4T1 cells were stably modified with lentiviral vectors to express the nuclear rupture reporter NLS-GFP (pCDH-NLS-copGFP-EF1-BlastiS, Addgene, # 132772), which is comprised of GFP fused to a nuclear localization sequence (NLS). Pseudoviral particles were produced by co-transfection of the lentiviral plasmid and lentiviral helper plasmids, including psPAX2 (Addgene, #12260) and pMD2.G (Addgene, #12259), into 293T cells using Lipofectamine LTX/PLUS (Invitrogen, 15338030) following manufacturer's protocol. Lentivirus-containing supernatants were collected at 24 hours after transfection, and filtered through a 0.45 μm filter. 4T1 cells were seeded into 6-well plates so that they reached 70% confluency on the day of infection and transduced with the virus-containing supernatant in the presence of 8 μg mL^{-1} polybrene (Sigma-Aldrich). The viral solution was replaced with fresh culture medium, and cells were cultured for 24 hours before selection with 10 μg mL^{-1} of blasticidine S (Gibco, A1113903) for 10 days. After selection, cells were subcultured and maintained in the complete culture medium with 5 μg mL^{-1} of blasticidine S.

Cas9-stable BlaER1 cells were generated by transducing BLaER1 cells with a lentiviral Cas9 nuclease expression vectors containing a human codon-optimized version of *S. pyogenes* Cas9 nuclease under the control of hCMV promoter and the fluorescent protein mKate2 (Horizon Discovery). 48 h after transduction, $mKate2^{+}$ cells were FACS sorted, expanded, and validated for stable Cas9 expression by Western blot using anti-Cas9 antibody (Santa Cruz Biotech, sc-517386). Using the Neon Transfection System (ThermoFisher Scientific), 2.5×10^{5} $Cas9^{+}$ BlaER1 cells were transfected (1400 V - Width 20 - 1 pulse) with 4.7 mM of STING-specific gRNA (Horizon Discovery) and then cultured in 3 mL of complete RPMI medium. 48h after transfection, cells were sorted into 96-well plates (1 cell/well) using BD FACSMelody™ Cell Sorter (BD Biosciences). 2 to 3 weeks after sorting, 12 to 14 clones were selected and expanded for 96h before assessing knockout efficiency by Western blot. Pseudoviral particles were produced by co-transfection of the lentiviral plasmid and lentiviral packaging/envelope plasmids, including pRRE (Addgene, #12251), pMD2.G and pRSV-REV

(Addgene, #12253) into 293T cells. Lentivirus-containing supernatants were collected at 24 hours after transfection, and filtered through a 0.45 μm filter. The virus-containing supernatant was added to 1 $\times 10^5$ BLaER1 cells with 2 μg mL^{-1} polybrene and were spin-transduced by centrifugation at 800 ×g for 45-60 min at 32°C. After centrifugation, cells were resuspended and seeded in a 24-well plate. After 24 h incubation with the viral particles, the virus-containing supernatant was removed and exchanged to fresh complete RPMI. After the third passage, positively transduced cells were selected with 4 μg mL^{-1} puromycin for 7 days.

EV purification, characterization and labelling

Preparation of conditioned medium from cultured cells for EV isolation was described above. For tissue explant culture, freshly dissected glioma or PDAC tumors from de-identified patients were cut into millimeter-sized pieces and cultured overnight in RPMI supplemented with 1× P/S, and the conditioned medium was collected for EV isolation and purification.

EV isolation and purification was performed by sequential ultracentrifugation as previously described.[33,34] In brief, the conditioned medium of the cultured cells or tumor explants was sequentially centrifuged at 500g for 10 min, at 3,000g for 20 min and then at 12,000g for 20 min. EVs were pelleted by ultracentrifugation of this supernatant at 100,000g for 70 min and washed with PBS once. EVs were then collected by ultracentrifugation at 100,000g for 70 min and resuspended in PBS. The protein concentration of EVs in PBS was measured by BCA Protein Assay Kit (Thermo Scientific, 23225). EV size and particle number were analyzed using the LM10 nanoparticle characterization system (NanoSight, Malvern Instruments). 5μl of EVs in PBS (0.1 μg μL^{-1}) were negatively stained with uranyl acetate (1.5%) and observed with a transmission electron microscope (JEM-1400, JEOL Ltd.) operating at 100 kV. Images were captured on a Veleta 2k × 2k charge-coupled device camera (Olympus-SIS).

For biodistribution studies, 25 μg of EVs, or an equivalent volume of PBS, were first gently mixed with 1 μL of CellVue dye (NIR815 or Burgundy, LI-COR) diluted in 125 μL of Diluent C and incubated in the dark for 5 min; 62.5 μL of 35% bovine serum albumin (BSA, EMD Millipore, 12659) was added to the mixture to quench the labelling reaction and incubated for 1 min. The mixture was washed with PBS and EVs were pelleted by ultracentrifugation at 100,000g for 70 min, and then resuspended in PBS for downstream experiments. For *in vitro* uptake studies, 10 μg of AT_{EVs} or 20 μg of NT_{EVs} (carrying ~ 4 μg of EV_{DNA}), or an equivalent volume of PBS, were mixed with TOTO-3 Iodide (Invitrogen, T3604) with a final dye concentration of 0.1 μM in PBS and incubated in the dark for 20 min at room temperature. The mixture was washed with 20 mL of PBS twice to completely remove free dye and EVs were pelleted by ultracentrifugation at 100,000g for 70 min, and then resuspended in 400 μL of complete culture medium for downstream experiments.

EV_{DNA} extraction, characterization and digestion

EV_{DNA} was extracted using the QIAamp DNA mini kit (Qiagen) combined with the Agencourt AMPure XP Bead-based system (Beckman, A63881): 100 μL of EVs were lysed by 100 μL of Buffer AL (QIAGEN) containing 10 μL of proteinase K (QIAGEN) and incubated at 56°C for 10 min. Magnetic beads for EV_{DNA} extraction were prepared by mixing 100 μL of AMPure beads with 100 μL of poly (ethylene glycol) 8000 (Sigma-Aldrich, P2139) solution (20% in 15% NaCl solution) and 100 μL of isopropanol. Lysed EVs were then mixed with magnetic beads and transferred to DynaMag™-2 Magnet (Invitrogen, 12321D). After washing the beads adherent to the magnet with 80% of ethanol twice, EV_{DNA} was eluted from beads with 20 μL of molecular water. The quality and quantity of EV_{DNA} were analyzed using Nanodrop 2000c (Thermo Scientific) and Qubit™ dsDNA high sensitivity assay kit (Invitrogen, Q33231) following the manufacturer's instructions. The size distribution of EV_{DNA} fragments was determined using Agilent Genomic DNA ScreenTape assay by the Genomics Resources Core Facility at Weill Cornell Medicine.

EV_{DNA} was digested by Baseline-ZERO™ DNase (Lucigen, DB0715K) according to manufacturer's instructions. Reaction mixtures were prepared by mixing the EV solution containing 1 μg of EV_{DNA} with 1 μL of Baseline-ZERO DNase, 2 μL of 10× Baseline-ZERO DNase and RNase-Free water to a final volume of 20 μL. After incubation at 37°C for 30 min, the Baseline-ZERO DNase was inactivated by adding 2 μL of 10× Baseline-ZERO DNase Stop Solution and subsequent incubation at 65°C for 10 min.

For the observation of EV_{DNA}, 5μl of human AT_{EVs} or Baseline-ZERO DNase-pretreated AT_{EVs} in PBS (0.1 μg μL^{-1}) were absorbed to formvar carbon-coated nickel grids, fixed with 2% paraformaldehyde (PFA) for 10 min and immune-labelled with an anti-dsDNA antibody (Santa Cruz, sc-58749) in 0.2% Aurion BSA-c™ (Electron Microscopy Sciences, 25557), followed by 6 nm Aurion gold-labelled secondary antibody (Electron Microscopy Sciences). The samples were fixed in 2.5% glutaraldehyde in 0.1 M phosphate buffer, negatively stained with uranyl acetate and observed with a transmission electron microscope (JEM-1400, JEOL Ltd.) operating at 100 kV. Images were captured on a Veleta 2k × 2k charge-coupled device camera (Olympus-SIS). Alternatively, super-resolution d-STORM imaging of EV_{DNA} on single EVs were performed by immunofluorescence labelling of EVs with EV Profiler kit (ONI). Briefly, 1-2 μg of EVs per lane were loaded and fixed to the four-lane flow-cell chip after prewashing. Then, the EVs were blocked with blocking solution (2.5 % BSA in PBS) and stained with the specified antibodies. Chips were imaged using ONI Nanoimager. Images were acquired with the ONI light program, at least 2 different fields (>300 vesicles per field) per sample. Data analysis was performed through the ONI analysis tool (https://alto.codi.bio) according to the instruction, larger EVs were excluded from the analysis.

BrdU pulse chase study

Activated or non-activated T cells were cultured in medium with BrdU (Sigma B5002) (10μM) for 12hrs. Cells were washed with fresh medium twice and then cultured for 24 hrs or 72 hrs. The gDNA was isolated using QIAamp DNA mini kit (Qiagen) and the EV_{DNA} was isolated using Agencourt AMPure XP Bead-based system (Beckman, A63881).

The Blot-dot BrdU assay was adapted from a previous method.[77] Briefly, 4 μg of gDNA or EV_{DNA} was single-stranded by incubation with 10 volumes of 0.4 N NaOH solution for 30 min at room temperature and kept on ice to prevent annealing. The DNA solution was

placed on ice and neutralized by an equal volumeof 1M Tris HCl (pH 6.8). The single-stranded neutralized DNA (20ng/μL) was dot-blotted onto a HyBond-XL membrane (GE-Healthcare) and fixed using Auto Mode (12000 units) by ultraviolet cross-linker Stratalinker (Strat-agene, La Jolla, CA).

To visualize the BrdU signal, the membrane was incubatedwith mouse anti-BrdU monoclonal antibody (1:2,000 dilution, Made in Molecular Cytology Core Facility, Memorial Sloan Kettering Cancer Research Center) in buffer containing 20 mM TBST containing 1% nonfat milk for 1 h atroom temperature. Blocking was not necessary. The membrane was washed with TBS-T for 10 min (3 times) and incubated with a mouse-HRP secondary antibody with 3 times washes (20 min per wash). The membrane developed using the Pierce ECL Western Blotting Substrate (Thermo Fisher Scientific), and visualized using the Bio-Rad ChemiDoc XRS+ Imaging System.

In vitro education with T cell-derived EVs

DC2.4 cells were seeded at a density of 5×10^4 cells mL^{-1} per well in 0.5 mL of complete RPMI medium in a 24-well plate and treated with PBS, mouse AT_{EVs} or NT_{EVs} (containing 5 μg mL^{-1} of EV_{DNA}), or Baseline-ZERO DNase-pretreated AT_{EVs} after overnight incubation. The following day, DC2.4 cells in each group were harvested and reseeded at the same density in a 48-well plate. The procedure was repeated for 3 times in total and cells in each treatment group were collected for RNA extraction and RNAseq profiling.

6419c5 cells were seeded at a density of 5×10^4 cells mL^{-1} per well in 1mL of complete DMEM medium in a 12-well plate and treated with PBS, mouse AT_{EVs} or NT_{EVs} (containing 5 μg mL^{-1} of EV_{DNA}), or Baseline-ZERO DNase-pretreated AT_{EVs} after overnight incubation. The following day, tumor cells in each group were harvested and reseeded at the same density in a 12-well plate. The procedure was repeated 8 times and cells in each treatment group were collected for RNA extraction as well as characterizations of the proliferation rate, migration capacity and $EV_{protein}$, $EV_{particle}$, and EV_{DNA} productions.

Coculture of BMDCs and naïve T cells

For the alloactivation of naïve T cells, BMDCs isolated from C57BL/6 mice were seeded at a density of 1×10^6 cells mL^{-1} per well in 0.1 mL of complete RPMI medium in a round-bottom 96-well plate and treated with PBS, 20ng mL^{-1} of LPS, C57BL/6 mouse NT_{EVs} or AT_{EVs} (containing 5 μg mL^{-1} of EV_{DNA}), or Baseline-ZERO DNase-pretreated AT_{EVs}. 24 hours after stimulation, BMDCs in each group were treated with 50 μg mL^{-1} of mitomycin C (Sigma-Aldrich, M5353) at 37°C for 30 min to stop BMDC proliferation and subsequently washed with cold PBS for 5 times to completely remove mitomycin C. Naïve T cells isolated from BALB/c mice were labeled with 2 μM CFSE (Thermo Fisher Scientific, C34554) at 37°C for 20 min and washed with complete RPMI medium according to the manufacturer's instructions. CFSE-labeled T cells were added into pre-treated BMDC cultures at a density of 4×10^6 cells mL^{-1} per well in 0.1 mL of complete RPMI medium supplemented with 50 U mL^{-1} of IL-2 and cultured for 4 days. The percentage of proliferative T cells that were negative for CFSE labelling was measured by flow cytometry.

For the APP restoration assay on MHC-I/II DKO BMDCs, BMDCs isolated from NSG-MHC-I/II DKO mice were seeded at a density of 1×10^6 cells mL^{-1} per well in 0.1 mL of complete RPMI medium in a round-bottom 96-well plate and treated with PBS, 20ng mL^{-1} of LPS, or C57BL/6 mouse AT_{EVs} (containing 5 μg mL^{-1} of EV_{DNA}) with or without Baseline-ZERO DNase digestion. The following day, BMDCs in each group were incubated with 100 μg mL^{-1} of endotoxin-free OVA protein (InvivoGen, vac-pova) for 24 h in the presence of LPS, AT_{EVs} or DNase-digested AT_{EVs} and subsequently treated with 50 μg mL^{-1} of mitomycin C (Sigma-Aldrich, M5353) to stop further proliferation and washed with cold PBS for 5 times. Naïve T cells isolated from C57BL/6 mice were labeled with 2 μM CFSE (Thermo Fisher Scientific, C34554) and then added into OVA-pulsed BMDC cultures at a density of 4×10^6 cells mL^{-1} per well in 0.1 mL of complete RPMI medium supplemented with 50 U mL^{-1} of IL-2 and cultured for 4 days. The proliferative T cells and OVA-specific $CD8^+$ T cells were detected by CFSE dilution and PE-labeled H-2Kb/SINFEKL tetramer protein via flow cytometry.

Treatment of DC2.4 cells

DC2.4 cells were seeded at a density of 1×10^5 cells mL^{-1} per well in 1 mL of complete RPMI medium in a 12-well plate. After overnight incubation, cells were replenished with 1 mL of fresh medium with the addition of PBS, 5 ng mL^{-1} of recombinant IFN-γ (Biolegend, 575302), 2μM of SAR-20347 (MedChemExpress, HY-100895), mouse AT_{EVs} or NT_{EVs} (containing 5 μg mL^{-1} of EV_{DNA}), Baseline-ZERO DNase-pretreated AT_{EVs} (containing 5 μg mL^{-1} of EV_{DNA} before DNase treatment), combination of SAR-20347 (2μM) and IFN-γ (5 ng mL^{-1}), combination of SAR-20347 (2μM) and AT_{EVs}, 1 μM of ODN D-SL03 (Invivogen), 5 μg mL^{-1} of Poly (dA:dT) / LyoVec™, combination of A151 (2μM) and AT_{EVs}, combination of A151(2μM) and ODN D-SL03 (1 μM), or combination of A151(2μM) and Poly (dA:dT) / LyoVec™ (5 μg mL^{-1}). 24 hours after stimulation, DC2.4 cells in each treatment group were harvested and analyzed for H-2Kb (MHC-I) and I-A/I-E (MHC-II) expressions by flow cytometry.

EV_{DNA} and EV_{RNA} transfection with lipofectamine 3000

EV_{DNA} were isolated from 50μg of mouse AT_{EVs} with or without Baseline-ZERO™ DNase pre-digestion. EV_{RNA} was isolated from 1mg of AT_{EVs} using the RNeasy Plus Mini kit. 293T cells were seeded at a density of 2×10^5 cells mL^{-1} per well in 1 mL of complete DMEM medium in a 12-well plate to reach 70 – 90% confluence after overnight incubation. 1 μg of EV_{DNA} or EV_{RNA}, or equal volume of DNAse pre-digested EV_{DNA} samples were mixed with 3μL of Lipofectamine™ 3000 (Invitrogen, L3000001) in 100 μL of Opti-MEM™ I reduced serum medium (Gibco, 31985062) following manufacturer's instructions. 293T cells were replenished with 1mL of fresh complete DMEM medium containing the transfection mixture. 24 hours after incubation, 293T cells in each treatment group were harvested for total RNA extraction and RT-qPCR analysis.

Cell migration assays

24 transwell plates with 8.0 μm pores (Corning, CLS3428) were used to assess the migration ability of KPCY cells. 6419c5 cells were seeded at a density of 5×10^5 cells mL^{-1} per insert in 0.1 mL of DMEM medium supplemented with 0.1% BSA. 0.6mL of complete DMEM medium was used as chemoattractant on the bottom side of the chambers. After 36h, tumor cells that migrated through the other side of the membrane were quantified using crystal violet (Sigma-Aldrich). Alternatively, wound-healing assay was conducted by creating a scratch on the confluent 6419c5 cell surface with a 200 μl pipet tip in 12 well plates. Wells were imaged immediately after performance of the scratch, and every 3 hours until closure of the scratch was reached using an Olympus light microscope. Scratch size was quantified by ImageJ 1.48v and closure rate was determined as the negative slope of scratch sizes over time.

Gzmb inhibitor screening assay

Concentrations of Gzmb inhibitor IV (Sigma-Aldrich, 368056) were screened using the Granzyme B Inhibitor Screening Kit (Sigma-Aldrich, MAK209) following the manufacturer's instructions. 0.1, 1, 5, or 10μM of Gzmb inhibitor IV were incubated with Gzmb and Gzmb substrate in Gzmb assay buffer in 96 well flat clear bottom black plates (Corning, 3601). The fluorescence of cleaved substrate ((λ_{ex} = 380/ λ_{em} = 500 nm) was measured in kinetic mode for 30 min at 37°C using SpectraMax® M5 multi-mode microplate reader. The fluorescence at each time point was used to determine the slop of the Gzmb inhibition plot. Relative reduction of the slope of the Gzmb inhibition plot as compared to that of the reaction setting without Gzmb inhibitor IV was calculated as % relative inhibition. The optimal concentration that achieved over 95% relative inhibition of Gzmb upon the addition of the inhibitor and maintained over 80% relative inhibition within 6 hours, the incubation period utilized for *in vitro* uptake of T cell derived EV_{DNA} and AT_{EV}-induced nuclear rupture.

Subcellular distribution of T cell-derived EV_{DNA}

6419c5 or DC2.4 cells were seeded at a density of 5×10^4 cells mL^{-1} in 2 mL of complete medium in 35mm confocal dishes. After overnight incubation, cells were washed with PBS and stained with 5μg mL^{-1} of Hoechst 33342 (Invitrogen, H1399) in PBS for 15 min at room temperature. Subsequently, the cells were washed with PBS for 3 times and replenished with 1mL of complete medium containing AT_{EVs} or NT_{EVs} (containing 5 μg mL^{-1} of EV_{DNA}) pre-stained with TOTO-3 iodide, or an equivalent volume of PBS. After 6-hour incubation, live cells were imaged with a 63× oil objective on Confocal Microscope (Zeiss LSM 880).

Enzyme-linked immunosorbent assay

0.2 μg of mouse NT_{EVs} or AT_{EVs} were subjected to IFN-γ measurement using the mouse IFN-gamma quantikine ELISA kit (R&D Systems, MIF00) according to the manufacturer's instructions. IL-2 was measured in 0.25 μg of mouse T cell-derived EVs or activated T cell culture medium after EV depletion using the Mouse IL-2 ELISA Kit (ThermoFisher Scientific, BMS601).

Western blotting

Cell samples were lysed by a RIPA buffer (Thermo Scientific, 89900) supplemented with cOmplete™ Protease Inhibitor Cocktail (Sigma-Aldrich, 4693116001) and PhosSTOP™ (Sigma-Aldrich, 4693116001, 4906845001). The BCA protein assay kit was used to determine the protein concentration in samples according to the manufacturer's protocols. The protein solution was diluted by NuPAGE™ LDS Sample Buffer (4×) (Invitrogen, NP0007) that contained NuPAGE™ Sample Reducing Agent (Invitrogen, NP0004) and heated at 95°C for 5 min. Protein was separated by SDS–PAGE (Invitrogen, XP00100BOX), and then transferred to polyvinylidene difluoride membranes (Bio-Rad, 1620177). The membranes were blocked with 5% bovine serum albumin at room temperature for 1 h and then incubated with primary antibodies overnight at 4°C. The membranes were washed and further incubated with HRP-conjugated secondary antibodies (appropriately diluted) at room temperature for 1 h, then developed using the Pierce ECL Western Blotting Substrate (Thermo Fisher Scientific), and visualized using the Bio-Rad ChemiDoc XRS+ Imaging System. GAPDH was used as the control. Cumulative densitometric analyses of the western blotting images were performed by ImageJ 1.48v. All antibodies are listed in the key resources table.

RNA extraction and RT-qPCR analysis

Total RNA was extracted using the RNeasy Plus Mini kit (Qiagen, 74134) following the manufacturer's instructions. Total RNA was then subjected to RT–qPCR analysis and RNAseq as described below.

For RT-qPCR analysis, 100–500 ng of total RNA was used for cDNA synthesis using the iScript™ cDNA Synthesis Kit (Bio-Rad, 1708890) following the manufacturer's instructions. 500ng of cDNA were used for RT–qPCR reactions using SYBR Green Supermix (Bio-Rad, 1725271) and gene-specific primers. ACTB was used as an internal control. RT–qPCR was performed on a CFX384 Touch Real-Time PCR System (Bio-Rad), and data were analysed by CFX Manager v3.1 (Bio-Rad). The relative gene expression was quantified by $2^{-\Delta\Delta Ct}$ method.[78]

For relative copy number variation analysis, 10ng of EV_{DNA} were used for RT–qPCR reactions using SYBR Green Supermix and gene-specific primers. ACTB was used as an internal control. The relative copy number variation was quantified by $2^{-\Delta\Delta Ct}$ method. Primers used in RT–qPCR analysis are listed in Table S3.

Flow cytometry

~200 mg of tumor tissues and whole liver tissues were harvested and ground into single cell suspension after digestion with collagenase type I (200 U mL^{-1}, Gibco, 17018029), collagenase type IV (200 U mL^{-1}, Gibco, 17104019), and DNase I (100 μg mL^{-1}, Sigma-Aldrich, 11284932001) at 37°C for 45 min. Cell pellets were incubated with ACK Lysing buffer (Gibco, A10492-01) at room temperature for 5 min to remove red blood cells. Cervical lymph nodes were harvested and ground into single cell suspension after digestion with collagenase D (2mg mL^{-1}, Sigma-Aldrich, 11088858001) and DNase I at 37°C for 30 min. Collected cells were washed and diluted to 2×10^6 cells mL^{-1} with PBS containing 3% FBS and 1mM EDTA. 1mL of the cell suspension were centrifuged and stained at room temperature for 30 min by the addition of a cocktail of live/dead dye (LIVE/DEAD™ Fixable Near-IR Dead Cell Stain Kit, Invitrogen, L34975), TruStain FcX™ PLUS antibody (Biolegend, 156603), and fluorescence conjugated antibodies for 30min at 4°C in the dark. For intracellular cytokine staining, cells were washed, fixed and permeabilized using BD Cytofix/Cytoperm fixation/permeabilization kit (BD Biosciences, 554714) for 20 min at 4°C in the dark. Intracellular staining was performed using fluorophore-conjugated cytokine antibodies for 30 min at 4°C in the dark. After staining, cells were either sorted via BD FACSMelody™ Cell Sorter or analyzed via BD LSRFortessa or FACSymphony™ A5. All the data were acquired with a BD FACSDIVA v8.0.1 and analysed via FlowJo V10 (TreeStar). All antibodies are listed in the key resources table.

Tissue processing and immunofluorescence staining

For cryosections, fresh tissues were resected and rinsed in PBS, and fixed in 4% PFA overnight at 4°C, followed by dehydration with 15% and 30% sucrose solution, respectively, for 24h at 4°C. Subsequently, tissues were snap frozen in OCT compound (Sakura, 4583) on dry ice. OCT-embedded tissues were sectioned at 10-μm thickness using LEICA CM3050 S, and slides were stored in −80°C freezer or used immediately.

For sections of paraffin-embedded tissues, fresh tissues were rinsed in PBS, fixed in 4% PFA for 48 h at 4°C, and then rinsed in tap water and placed in 70% ethanol solution until paraffin-embedded. Paraffin-embedding was performed by the Electron Microscopy and Histology Core Facility at Weill Cornell Medicine. The paraffin-embedded tissues were sectioned at 7-μm thickness, and deparaffinized through xylene and serial dilutions of 100% to 75% ethanol and distilled water. For antigen retrieval, slides were placed in a jar containing sodium citrate and then placed in boiling water bath in a hot pressure cooker at low pressure for 30 min.

For immunofluorescence staining, cryosections or deparaffinized sections were processed through permeabilization with 0.1% Triton X-100 and blocking in 5% goat serum at room temperature for 1 h. Primary antibodies were incubated at 4°C overnight, and fluorescent secondary antibodies were incubated at room temperature for 1 h. Finally, the slices were mounted with Prolong® Diamond Antifade Mountant with DAPI (Invitrogen, P36962). Images were captured using Confocal Microscope (Zeiss LSM 880 or Zeiss LSM 800). All antibodies are listed in the key resources table.

Biodistribution assessment

For the whole-organ imaging, 25 μg of CellVue NIR815 labeled EVs resuspended in 100 μL of PBS, or an equivalent volume of mock EV labeling mixture, were retro-orbitally injected into naive or SB28 GBM-bearing or orthotopic 6419c5 PDAC-bearing C57BL/6 mice (female, 8-10 weeks old). At 24 h post-injection, mice were transcardially perfused with 30 mL of PBS. Subsequently, organs were collected and imaged using Odyssey CLx (LI-COR). Data quantification was performed using Image Studio v5.2.

For the biodistribution analysis in Icam-1 neutralized mice, InVivoMAb anti-mouse CD54 (BE0020-1, Clone: YN1/1.7.4) or InVivoMAb rat IgG2b isotype control (BE0090) from BioXCell were intraperitoneally injected into the mice at a dosage of 200 μg per mouse every other day starting on day 7 post intra-pancreatic injection of 6419c5 tumour cells for a total of 3 injections in C57BL/6 mice (female, 8-10 weeks old). One day after the last injection, 25 μg of CellVue NIR815 labeled AT_{EVs} resuspended in 100 μl of PBS, or an equivalent volume of mock EV labeling mixture, were retro-orbitally injected into mice treated with IgG control or anti-CD54 (Icam-1). At 24 h post-injection, mice were transcardially perfused with 30 mL of PBS. Subsequently, organs were collected and imaged using Odyssey CLx (LI-COR). Data quantification was performed using Image Studio v5.2.

For the biodistribution analysis at the cellular level, 25 μg of CellVue Burgundy labeled EVs resuspended in 100 μl of PBS, or an equivalent volume of mock EV labeling mixture, were retro-orbitally injected into naïve or orthotopic 6419c5 PDAC-bearing C57BL/6 mice (female, 8-10 weeks old). At 24 h post-injection, cervical lymph nodes and tumors were harvested for flow cytometry analyses.

Tumor models and *in vivo* treatments

For the orthotopic GBM model, 1×10^4 of SB28 cells in 2 μL of serum-free DMEM medium were intracranially injected into 8-week-old female C57BL/6 mice by the Antitumor Assessment Core Facility at MSKCC. Briefly, mice were anesthetized with isoflurane and placed into a stereotactic frame and a single midline incision was made to expose the cranium. A hole was drilled into the cranium above the left cerebral hemisphere using a precision power drill equipped with a fine bit at the following coordinates from bregma: +0.5 mm AP, +2.1 mm ML, and −3.2 mm DV. Upon exposing the underlying dura, tumor cells were injected into the right striatum using a micro-pump injector and a 5-μL Hamilton syringe equipped with a 33-gauge needle for 2 min at a rate of 1 μL min^{-1}. Cells were allowed to settle for 5 min followed by slow needle withdrawal. One week after tumor inoculation, mice were randomized blindly into different treatment groups, and the investigator was blinded to the group allocation during the animal experiments. PBS (i.v.), 50 μg of NT_{EVs} or 25 μg of AT_{EVs} (containing 10 μg of EV_{DNA}, i.v.) were given at the respective schedules every 3 days. Tumor growth was monitored by intraperitoneal (i.p.) injection of 100 μL of D-luciferin (20 mg/mL, Perkin Elmer) followed by

bioluminescent analysis using an IVIS® Kinetics Optical System (Perkin Elmer). The increase of tumor volumes was calculated as luminescence intensities (photon/sec) over the initial. At the indicated time point after 5 treatments, 3-5 mice in each group were sacrificed for the GBM collection, followed by flow cytometry analysis and immunofluorescence staining. For survival studies, the final endpoint achieved when one of the following conditions applied: drastic weight loss greater than 10% within 1 week, or clear signs of distress were detected, such as loss of appetite, dehydration, inactivity, difficulty breathing, hunched posture and withdrawal from other mice.

For the subcutaneous PDAC model, 5×10^5 of 6419c5 cells in 50 μL of Corning Matrigel matrix (Corning, 354248) were subcutaneously injected into the right flank of 8-week-old female C57BL/6 mice. 4 days after tumor inoculation, mice were randomized blindly into different treatment groups, and the investigator was blinded to the group allocation during the animal experiments. Each mice received one intratumoral injection of PBS or 25 μg of AT_{EVs} (containing 10 μg of EV_{DNA}) in the volume of 30 μL every 3 days for in total 6 doses. Tumor growth was monitored by measuring the tumor size with a digital caliper using the formula: tumor volume (mm^3) = width (in mm)^2 × length (in mm)/2. Mice were euthanized 9 days after the final treatment. Tumors were harvested for flow cytometry analysis and bulk RNAseq. The maximal tumor size in mice that was permitted by Weill Cornell Medicine IACUC is 2 cm in any one dimension, and this limit was not exceeded in any of the experiments.

For the orthotopic PDAC model, 5×10^4 of 6419c5/Luc cells in 50 μL of Corning Matrigel matrix were injected into the tail of the pancreas of 8-week-old female C57BL/6 mice. Briefly, mice were anesthetized with isoflurane and placed in supine position. A midline incision was made to exteriorize the spleen and pancreas for tumor cell injections. Then, the abdominal wall and skin were closed. One week after tumor inoculation, mice were randomized blindly into different treatment groups, and the investigator was blinded to the group allocation during the animal experiments. PBS (i.v.), 25 μg of AT_{EVs} (containing 10 μg of EV_{DNA}, i.v.) + 200 μg polyclonal rat IgG (Bioxcell, BE0094) (i.p.), 200 μg of anti-mouse PD1 (clone RMP1-14, Bioxcell, BE0146) (i.p.), and 25 μg of AT_{EVs} (i.p.) + 200 μg of anti-mouse PD1 (i.p.) were given at the respective schedules. Tumor growth was monitored by IVIS® Kinetics Optical System in the same way as the SB28 GBM model. At indicated time points after 5 treatments, 3-5 mice in each group were sacrificed. The primary tumor tissues or livers were harvested for flow cytometry analysis and immunofluorescence staining. For survival studies, the final endpoint achieved following the same protocol as described in the SB28 GBM model.

For the orthotopic PyMT breast cancer model, 1×10^6 of PyMT-T^{lo} cells in 50 μL of PBS were injected into the mammary fat pad of 8-week-old FVB/NJ mice. 4 weeks after tumor inoculation, mice were randomized blindly into different treatment groups, and the investigator was blinded to the group allocation during the animal experiments. PBS (i.v.), 25 μg of AT_{EVs} (containing 10 μg of EV_{DNA}, i.v.) + 200 μg polyclonal rat IgG (i.p.), 200 μg of anti-mouse PD1 (i.p.), and 25 μg of AT_{EVs} (i.p.) + 200 μg of anti-mouse PD1 (i.p.) were given at the respective schedules. Tumor growth was monitored by a digital caliper. 2 days after 3 treatments, 3 mice in each group were sacrificed for flow cytometry analysis. For survival studies, the final endpoint achieved when the tumor size reached 1000 mm^3.

For the *in vivo* education of T cell-derived EVs, naïve C57BL/6 mice (female, 8 weeks old) received i.v. injections retro-orbitally of PBS, 50 μg of NT_{EVs} or 25 μg of AT_{EVs} (containing 10 μg of EV_{DNA}), or 25 μg of Baseline-ZERO DNase-pretreated AT_{EVs} every other day for in total 3 doses. Subsequently, cervical lymph nodes were subjected to FACS sorting of $CD45^+CD11b^-CD11c^+$ DCs for total RNA extraction and RNAseq profiling.

For the cross-strain study, naïve C57BL/6 mice (female, 8 weeks old) received one i.v. injection of PBS, 25 μg of AT_{EVs} (containing 10 μg of EV_{DNA}) or 25 μg of Baseline-ZERO DNase-pretreated AT_{EVs} derived from BALB/c mice (female, 10-12 weeks old) retro-orbitally. Similarly, naïve BALB/c mice (female, 8 weeks old) received one i.v. injection of PBS, 25 μg of AT_{EVs} or 25 μg of Baseline-ZERO DNase-pretreated AT_{EVs} derived from C57Bl/6 mice (female, 10-12 weeks old) retro-orbitally. At 24 h post-injection, cervical lymph nodes from treated C57BL/6 or BALB/c were harvested for flow cytometry characterization for expressions of H2-Kb (MHC-I haplotype for C57BL/6) versus H2-Kd (MHC-I haplotype for BALB/c) on DCs.

RNAseq and bioinformatic analysis

Total RNA was extracted from PyMT cells, *in vitro* or *in vivo* educated DC2.4, lymph node DCs, 6419c5 cells or bulk 6419c5 tumors following the above protocol. The RNA quantity and quality was determined by Nanodrop 2000c and Agilent 2100 Bioanalyzer (Agilent Technologies). Illumina stranded total RNA preparation with Ribo-Zero Plus was conducted for *in vivo* educated lymph node DC RNA samples and sequenced by Illumina NovaSeq X Plus. TruSeq stranded mRNA library preparation was utilized for all the other samples and sequenced using Illumina Novaseq 6000 with an intended depth of 30 million reads per sample. All library preparations and RNA sequencing were performed in the Genomics Resources Core Facility at Weill Cornell Medicine.

The raw sequencing reads in BCL format were processed through bcl2fastq 2.19 (Illumina) for FASTQ conversion and demultiplexing. RNA reads were aligned and mapped to the mm9 mouse reference genome by TopHat2 (version 2.0.11) (http://ccb.jhu.edu/software/tophat/index.shtml), and transcriptome reconstruction was performed by Cufflinks (version 2.1.1) (http://cole-trapnell-lab.github.io/cufflinks/). The abundance of transcripts was measured with Cufflinks in fragments per kilobase of exon model per million mapped reads (FPKM). The QC reports for all RNAseq experiments can be found in Table S4. Gene expression profiles were constructed for differential expression and PCA analyses using the DESeq2 package (https://bioconductor.org/packages/release/bioc/html/DESeq2.html) of the R program. For differential expression analysis, pairwise comparisons between two or more groups were performed using parametric tests where read counts follow a negative binomial distribution with a gene-specific dispersion parameter. Corrected *P*-values were calculated based on the Benjamini–Hochberg method to adjust for multiple testing. Variance stabilizing transformed counts were used to make the PCA plot with PCAGO or 'pcaExplorer' package of the R program.

Normalized counts data from DESeq2 were used to make z-score heat maps using Heatmapper. Volcano plots were prepared using GraphPad Prism 8. Genes with absolute number of log_2FC larger than 0.5 were subjected to GSEA with Kegg and Reactome gene sets using GSEA v4.2.2. Venn diagrams were utilized to identify overlapping genes that were significantly upregulated (P-value < 0.05) in DC2.4 cells and 6419c5 cells after *in vitro* education with AT_{EVs} compared with the PBS treatment. Loci of these genes were highlighted in each chromosome using ChromoMap v0.4.1.[79]

WGS and bioinformatics analysis

The gDNA from non-activated or activated T cells were extracted using AllPrep DNA/RNA mini kit (Qiagen, 80204) following manufacturer's instructions. T cell-derived EV_{DNA} was extracted according to the above protocol. WGS libraries were prepared using the Truseq DNA PCR-free Library Preparation Kit (Illumina) in accordance with the manufacturer's instructions. Briefly, 1μg of DNA was sheared using a Covaris LE220 sonicator (adaptive focused acoustics). DNA fragments underwent bead-based size selection and were subsequently end-repaired, adenylated, and ligated to Illumina sequencing adapters. Final libraries were quantified using the Qubit Fluorometer (Life Technologies) or Spectromax M2 (Molecular Devices) and Fragment Analyzer (Advanced Analytical) or Agilent 2100 BioAnalyzer. Libraries were sequenced on an Illumina Novaseq6000 sequencer using 2x150bp cycles, targeting 40x coverage per base.

For the alignment and variant calling, paired-end 150bp reads were aligned to the mm9 mouse reference using the Burrows-Wheeler Aligner (BWA-MEM v0.7.15) and processed using the GATK best-practices workflow that includes marking of duplicate reads by the use of Picard tools (v2.4.1, http://picard.sourceforge.net), and base quality score recalibration (BQSR) via Genome Analysis Toolkit (GATK v3.5).[80,81] The QC reports for all WGS experiments can be found in Table S4. For the circos plot, average coverages were calculated with samtools mpileup command and bin sizes of 100,000 bp, then plotted with circos (v.0.69.9) in python (python-circos v0.3.0), with a max value of 100 and min value of 0. The copy number variation between AT_{EV}- and NT_{EV}-associated DNA was conducted with CNVkit v.0.9.7 using alignments for non-activated T cell-derived EV_{DNA} as the control and default settings.

Sample preparation for mass spectrometry (MS), MS data processing and proteomics data analysis

EV samples were prepared for liquid chromatography with tandem mass spectrometry (LC-MS/MS) analysis at the Rockefeller University Proteomics Resource Center as previously described.[34] Briefly, 5 μg of EV samples were dried by vacuum centrifugation and re-dissolved in 30-50μL 8M urea/50mM ammonium bicarbonate/10mm DTT. Following lysis and reduction, proteins were alkylated using 20 or 30mM iodoacetamide (Sigma-Aldrich). Proteins were digested with Endopeptidase Lys-C (Wako) in < 4M urea followed by trypsination (Promega) in < 2M urea. Peptides were desalted and concentrated using Empore C18-based solid phase extraction prior to analysis by high resolution/high mass accuracy reversed phase (C18) nano-LC-MS/MS. Peptides were separated on a C18 column (12 cm / 75 mm, 3 mm beads, Nikkyo Technologies) at 200 or 300 nl min^{-1} with a gradient increasing from 1% Buffer B/95% buffer A to 40% buffer B/60% Buffer A in typically 90 or 120 min (buffer A: 0.1% formic acid, buffer B: 0.1% formic acid in 80% acetonitrile). Mass spectrometers (Q-Exactive-HF and LUMOS) were operated in data dependent positive ion mode.

Generated LC-MS/MS data was processed using Proteome Discoverer/Mascot v2.5. Mouse or human data was queried against UniProt's mouse or human cell culture database concatenated with Trypsin/Lys-C sequences. Identified proteins without contaminants were utilized for subsequent analysis.

Abundance (average area of the 3 most intense peptides for a protein group) of identified proteins were evaluated by principal component analysis (PCA) using proteiNorm[82] with default settings for consistency in the replicates. Fold changes (FCs) and significance of protein abundance were calculated by using raw data log_2 transformation and normalization, followed by missing data imputation, F-test, log_2FC, and P-value determination.[83] Heatmaps were generated based on normalized abundance of identified proteins using the online analysis tool Heatmapper[84] and Excel. Venn diagrams analyzed at the Bioinformatics & Evolutionary Genomics website were used to identify proteins that were uniquely expressed on mouse or human AT_{EVs} as compared to mouse or human NT_{EVs} as well as overlapping proteins that were distinctively expressed on mouse and human AT_{EVs}. Volcano plots were prepared using GraphPad Prism 8. Proteins with the absolute number of log_2FC of protein abundance larger than 0.5 were used for gene set enrichment analysis (GSEA) with Kyoto Encyclopedia of Genes and Genomes (Kegg) and Reactome gene sets from the Molecular Signatures database (MSigDB v2023.2) using GSEA software (v4.2.2).

Nanopore sequencing and bioinformatics analysis

Mouse primary BMDCs were treated with either PBS or AT_{EVs} (containing 10ug/mL of EV_{DNA}) for 24 hours, followed by washing and collection of cell pellets. In parallel, 293T cells were treated with either PBS or lentiviral vector (Addgene# 200961) under the same conditions and similarly processed. The collected cell pellets were subsequently subjected to gDNA isolation using NEB Monarch HMW DNA Extraction Kit (cat#T3050) following manufacturer's protocol provided for standard input 1M cells. DNA was quantified on Invitrogen Qubit (Cat# Q33231) and assessed on the Agilent Fragment Analyzer Large Fragment 50kb kit (Cat# DNF-464-0500). Fragments were found to have an average of length of 70kb. Samples were sheared using Covaris gTube 6-20kb (cat #520079) following protocol to obtain 20kb fragments.

DNA Libraries were prepared with the SQK-LSK114 gDNA Ligation Sequencing Kit and sequenced with FLO-PRO114M flow cells (Oxford Nanopore Technologies). Real-time basecalled reads were produced with MinKNOW Version 24.06.15 and aligned separately with minimap2 v2.28 to the UCSC hg38 reference genome (https://doi.org/10.1101/gr.159624.113), UCSC mm10 reference genome and viral vector (LentiGuide-GFP.fa for BMDCs, Addgene# 200961 for the 293T cells). Selected gene coordinates were

queried the UCSC genome browser (https://genome.ucsc.edu/cgi-bin/hgGateway). Reads associated with these genes were extracted with samtools v1.21. pysam v0.22.1 was used to extract left and right soft-clipped ends. Soft-clipped ends greater than or equal to 50 bp from either AT_{EVs} or viral vector conditions were aligned to soft-clipped ends from the PBS condition with minimap2 v2.28. The ratio between the number of unaligned soft-clipped ends and total DNA count was then calculated to score gene integration.

QUANTIFICATION AND STATISTICAL ANALYSIS

Unless otherwise stateted, statistical significance was determined by two-tailed, unpaired Student's t-test, one-way ANOVA with post hoc Tukey's test, ordinary two-way ANOVA with Turkey's multiple comparisons, or log rank test using GraphPad Prism 8. The P-value and FDR q-value were determined by Kolmogorov–Smirnov test for GSEA. P-value < 0.05 was considered statistically significant. All values are mean ± standard deviation (SD). The number of independent biological replicates for each experiment and the sample size of each experimental group or condition are provided in the figure legends. ImageJ 1.48v was used for image processing and analysis.